



Application of Synchrotron X-Ray Imaging and Diffraction in Additive Manufacturing: A Review

Naying An¹ · Sansan Shuai¹ · Tao Hu¹ · Chaoyue Chen¹ · Jiang Wang¹ · Zhongming Ren¹

Received: 31 May 2021 / Revised: 13 August 2021 / Accepted: 17 August 2021 / Published online: 9 October 2021
© The Chinese Society for Metals (CSM) and Springer-Verlag GmbH Germany, part of Springer Nature 2021

Abstract

Additive manufacturing (AM) is a rapid prototyping technology based on the idea of discrete accumulation which offers an advantage of economically fabricating a component with complex geometries in a rapid design-to-manufacture cycle. However, various internal defects, such as balling, cracks, residual stress and porosity, are inevitably occurred during AM due to the complexity of laser/electron beam-powder interaction, rapid melting and solidification process, and microstructure evolution. The existence of porosity defects can potentially deteriorate the mechanical properties of selective laser melting (SLM) components, such as material stiffness, hardness, tensile strength, and fatigue resistance performance. Synchrotron X-ray imaging and diffraction are important non-destructive means to elaborately characterize the internal defect characteristics and mechanical properties of AM parts. This paper presents a review on the application of synchrotron X-ray in identifying and verifying the quality and requirement of AM parts. Defects, microstructures and mechanical properties of printed components characterized by synchrotron X-ray imaging and diffraction are summarized in this review. Subsequently, this paper also elaborates on the online characterization of the evolution of the microstructure during AM using synchrotron X-ray imaging, and introduces the method for measuring AM stress by X-ray diffraction (XRD). Finally, the future application of synchrotron X-ray characterization in the AM is prospected.

Keywords Additive manufacturing · Synchrotron X-ray imaging · X-ray diffraction · Defect formation · Mechanical properties · Residual stress

1 Introduction

Additive manufacturing (AM), commonly known as 3D printing, was one of the main rapid prototyping technologies developed in the 1990s [1]. It usually uses metal powder as the raw material, pre-spreads the powder material on the substrate area through the pre-layering process of the computer-aided design (CAD) model, and then uses the

high-energy beam to melt the metal powder layer by layer, and finally form the artifacts [2, 3]. Additive manufacturing technology can not only meet the processing requirements of special parts in the manufacturing process, but also can quickly produce samples, molds or models of new products without the restriction of the geometric shape of parts, and improve production efficiency. Therefore, the emergence of AM has provided new impetus for the development of manufacturing technology in many fields such as aerospace, foundry industry, architecture, and medical equipment.

However, producing defect-free components by AM is still challenging due to the lack of a fully understanding of the underlying physical and metallurgical process of AM. The process is usually affected by many factors, such as laser energy input and scan speed, scan strategy, powder material, powder size and morphology. The aforementioned factors might lead to form the defects of porosities, incomplete fusion holes, cracks, and impurities, etc. These defects are detrimental to a fabricated part in terms of its mechanical and physical properties, which in turn limits the

Available online at <http://link.springer.com/journal/40195>.

- ✉ Sansan Shuai
shuaisansan.cool@163.com
- ✉ Jiang Wang
jiangwang@i.shu.edu.cn
- ✉ Zhongming Ren
zmren@staff.shu.edu.cn

¹ State Key Laboratory of Advanced Special Steels, School of Materials Science and Engineering, Shanghai University, Shanghai 200444, China

application of AM [4, 5]. The precise characterization of the inner defects in fabricated parts is highly expected. In addition, the structure of the AM parts is usually complex, which leads to a large detection blind area in the traditional inspection process. For AM parts, traditional destructive detection can no longer meet the requirements. Advanced non-destructive inspection methods are highly desirable, especially for parts with complex structure and high precision. However, the nonuniformity of microstructure and the anisotropy of defects in parts brings challenges to qualitative and quantitative inspection.

Non-destructive detection includes traditional ultrasonic detection [6], X-ray detection, eddy current detection [7] and so on. Among them, X-ray detection has advantages for the detection of complex samples via radiography (two dimensional—2D) or tomography (three dimensional—3D) as shown in Fig. 1. Two-dimensional imaging includes direct radiography, which shows the structure and defects of the

parts on the display screen by making use of the difference in X-ray absorption of materials with different thicknesses or densities. While 3D tomography is also known as X-ray computed tomography (XCT), which could obtain a 3D volume or surface rendering by reconstructing a whole set of 2D projections to series of slices containing the micro/macro-structure information of the components [8]. It can intuitively and accurately characterize the structure of objects and has a wide range of applications in pore characterization, size measurement and reverse modeling [9].

Since AM is essentially a non-equilibrium thermodynamic process, parts are inevitable during the process of rapid heating and cooling, there will be problems such as non-uniform microstructure, metallurgy defect, residual stress as well as cracks. The high residual stress gradient will also result in deformation or microcracks, impacting the performance of the printed components [10, 11]. Measuring residual stress is still a challenge, and there is no method to

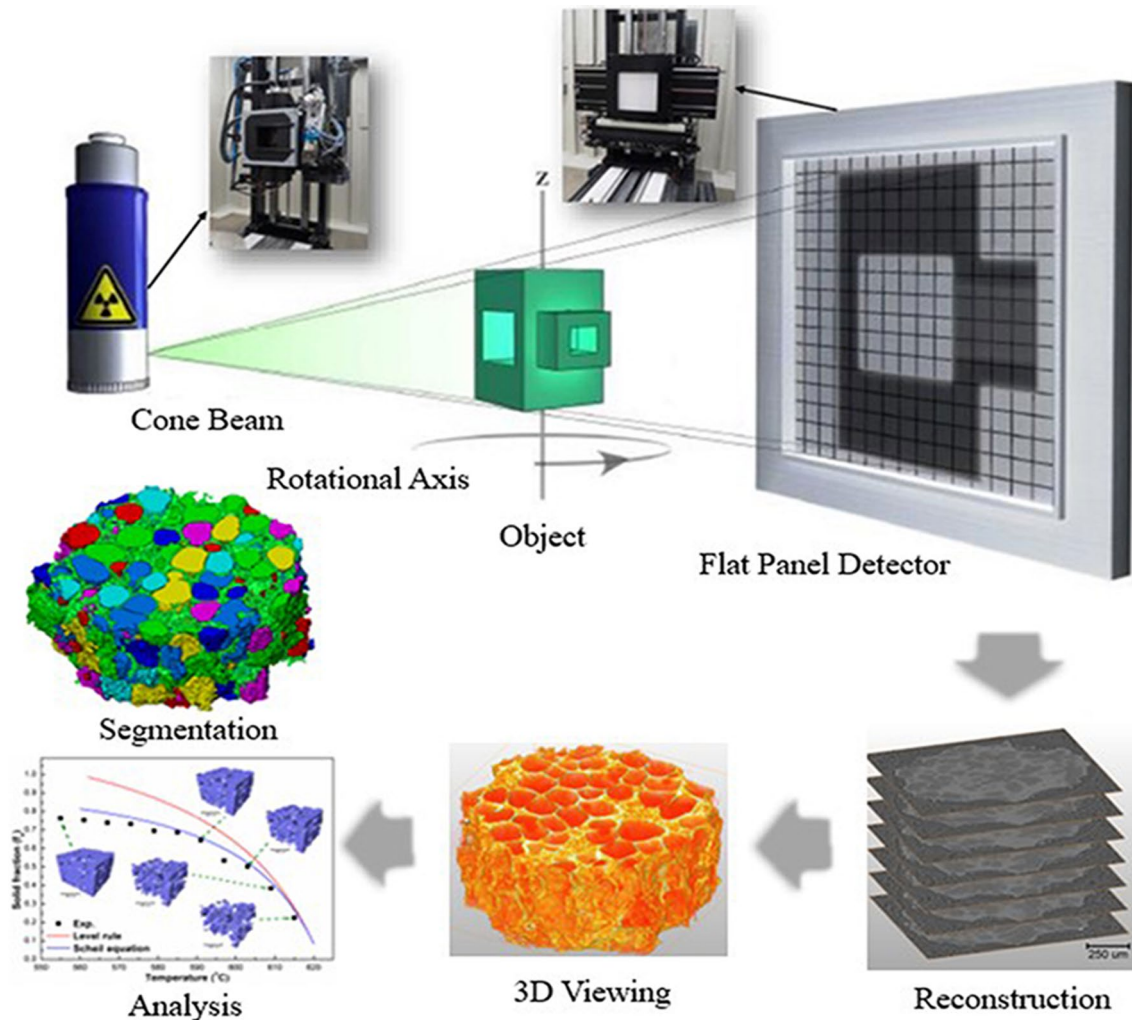


Fig. 1 Schematic of the XCT process

measure its value directly at present. The residual stress in the component is mainly evaluated via indirect methods, that is, through the change of physical properties caused by lattice distortion to know the residual stress. However, because the residual stress state of AM parts is complex, it is necessary to use non-destructive testing technology, including X-ray diffraction (XRD), synchrotron radiation [12], neutron diffraction [13], ultrasonic [14] and so on. Among these, XRD is considered to be the most effective and extensive method to measure residual stress because of its advantages such as quantitative measurement, accuracy and low cost. In addition, XRD also plays an important role in the identification of crystalline materials, preferred orientations, particle size and structure randomness of AM parts [15, 16].

This paper provides an overview of the application of synchrotron X-ray imaging and diffraction in AM, which has been divided into four sections. The first section briefly presents the use of XCT to characterize metal powder, microstructure, dimensional metrology, defects and mechanical properties of AM parts. Section 2 draws together research in the area of in situ analysis of microstructure evolution during the AM process. The measurement of residual stress on AM parts by XRD is explained in the third section. Finally, the current challenges and future applications will be addressed in the final section of the paper.

2 Application of XCT in Additive Manufacturing

2.1 Characterization of Metal Powder

Among the process of AM, the properties of the raw metal powders affect the ultimate performance of the part to a certain extent. Therefore, the characters of raw powder materials are studied, so as to optimize AM technology and improve the quality of AM parts. At present, the study of metal powder is mainly focused on the preparation process of powder, the particle size of the microstructure and impurity content, the morphology and phase of the powder, etc. However, the common characterization methods such as scanning electron microscope (SEM), transmission electron microscope (TEM) and differential scanning calorimetry (DSC) can only characterize the micro-morphology and microstructure of a certain cross section of the powder, but cannot analyze the overall properties of the powder in an all-round way. Therefore, using synchrotron or laboratory X-ray tomography can better characterize the 3D microstructure of the powder, thereby promoting the subsequent formation process.

Zhao et al. [17] characterized the surface and internal pores of gas atomized Ti6Al4V alloy powder by synchrotron X-ray imaging. The results showed that with the decrease

in the particle size of the powder, the surface of the powder changed gradually from sags and crested to smooth surface, and the internal pores of the powder gradually decreased. In addition, the porosity and pore size of the powder enlarge with the increase in the particle size of the powder, as shown in Fig. 2. It also shows that the 3D morphology of the powder is helpful to accurately represent the location and size of the defects, and can calculate the volume, surface area and other information.

Further, Zhou et al. [18] characterized the powder morphology by XCT and SEM. The results showed that compared with the 2D slice, the XCT results more closely matched measurements made of SEM images of powder particles. In recent years, scholars have focused on the effect of hollow powder in the AM process. Wang et al. [19] reconstructed the 3D morphology of the cavity in AlSi10Mg particles by XCT. They found that the cavity in the particles significantly affected the heat conduction of the material, thus reducing the sintering density (Fig. 3).

The aforementioned results show that XCT technology has displayed the ability to comprehensively characterizing the 3D morphology of raw powder materials, which lays a foundation for further studies of the influence of powder characteristics in the AM process.

2.2 Microstructure

In addition to qualitative and quantitative characters of raw powder materials, the 3D microstructure of AM parts can also be characterized using XCT. AM parts often have

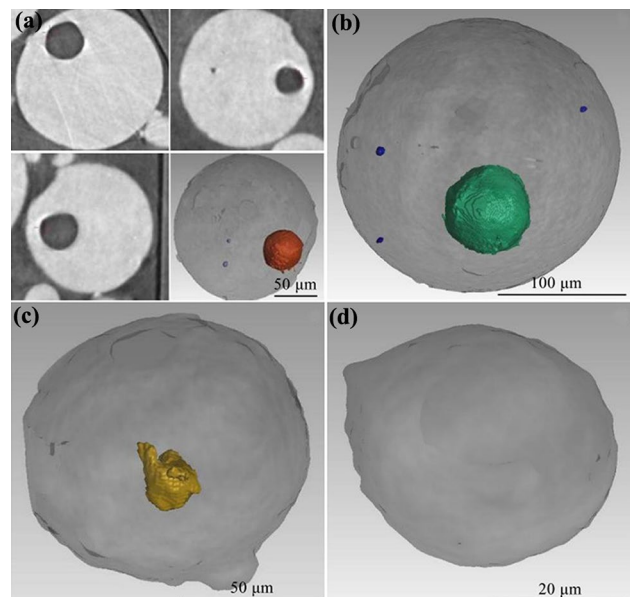


Fig. 2. Three-dimensional reconstructed topography of powders with different particle sizes: **a** 200 μm ; **b** 210 μm ; **c** 95 μm ; **d** 40 μm [17]

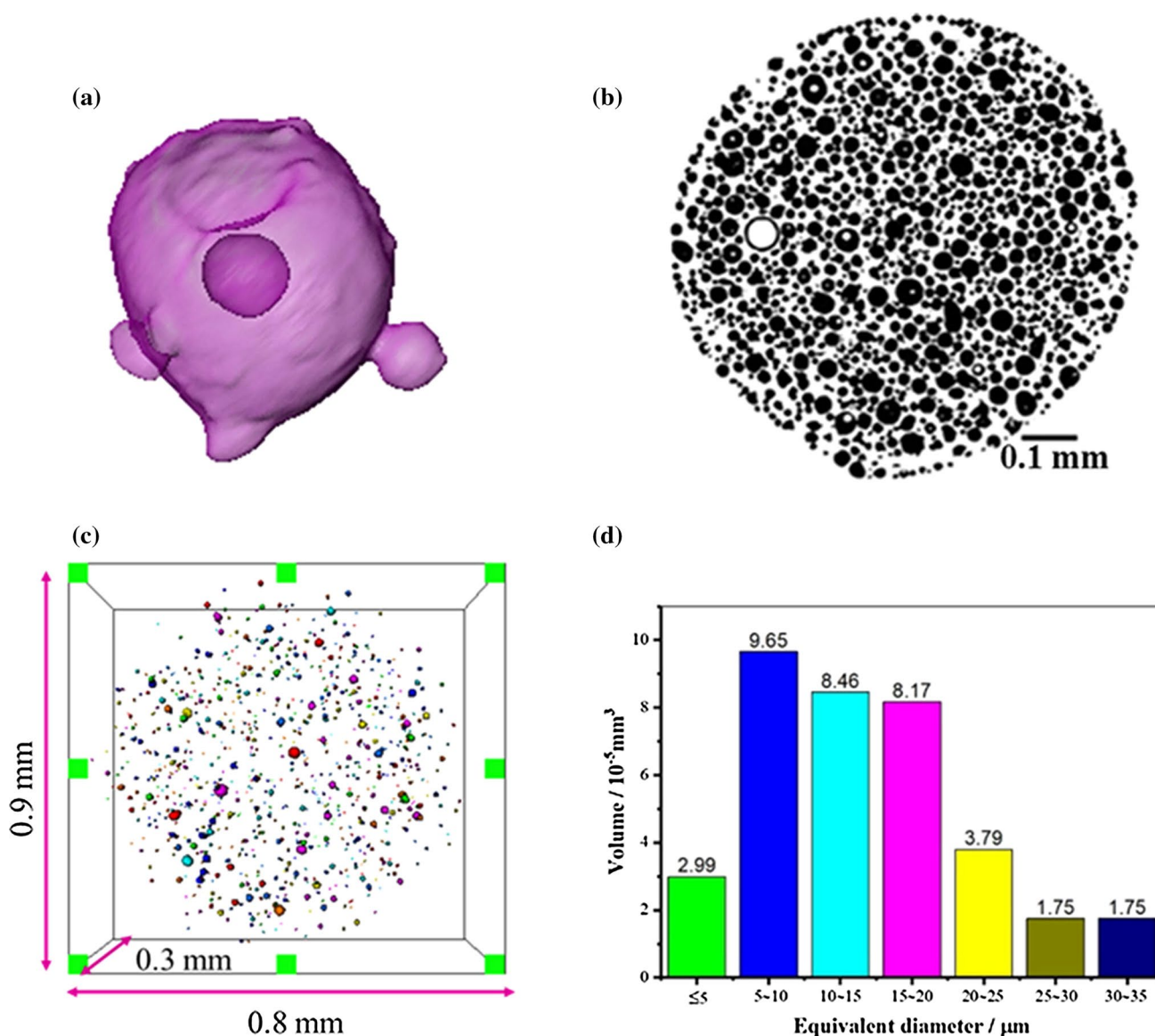


Fig. 3 a Cavities in AlSi10Mg particles; b 2D slices; c 3D reconstruction structure of cavities in particles; d distribution of the cavity size [19]

complicated microstructures. Based on the characteristics of computed tomography (CT) imaging, the reconstructed 3D image includes all the internal features of AM parts, which enables the internal structure and defects of the parts to be clearly characterized.

In an analysis of the pure titanium implants in electron beam additive manufacturing (EBAM), Ahn et al. [20] found that the commercial purity (CP) titanium implant is composed of an inner frame and an inner hole, on which about 80 μm titanium powder was attached, and the inner pore size increased rapidly with the increase in porosity. Figure 4 shows CP-Ti implants with different porosities. Wen et al. [21] used XCT to characterize the Ti–Al alloy lattice structure printed by SLM. The XCT method

realized the visualization of AM complex lattice structure and provided strong technical support and the basis for the reliability analysis of lattice structures. Recently, Carneiro et al. [22] proposed a new technology of combining AM with investment casting, and XCT was used to characterize the macro-scale structure and defects in the lattice samples. This method is of great significance to reform the structure of the metal lattice.

The above conclusions show that CT is a powerful method to characterize the morphology and internal structure of AM parts. In the future, the combination of CT and electron backscattered scattering detection (EBSD) data will provide more possibilities in order to better improve the performance of AM parts.

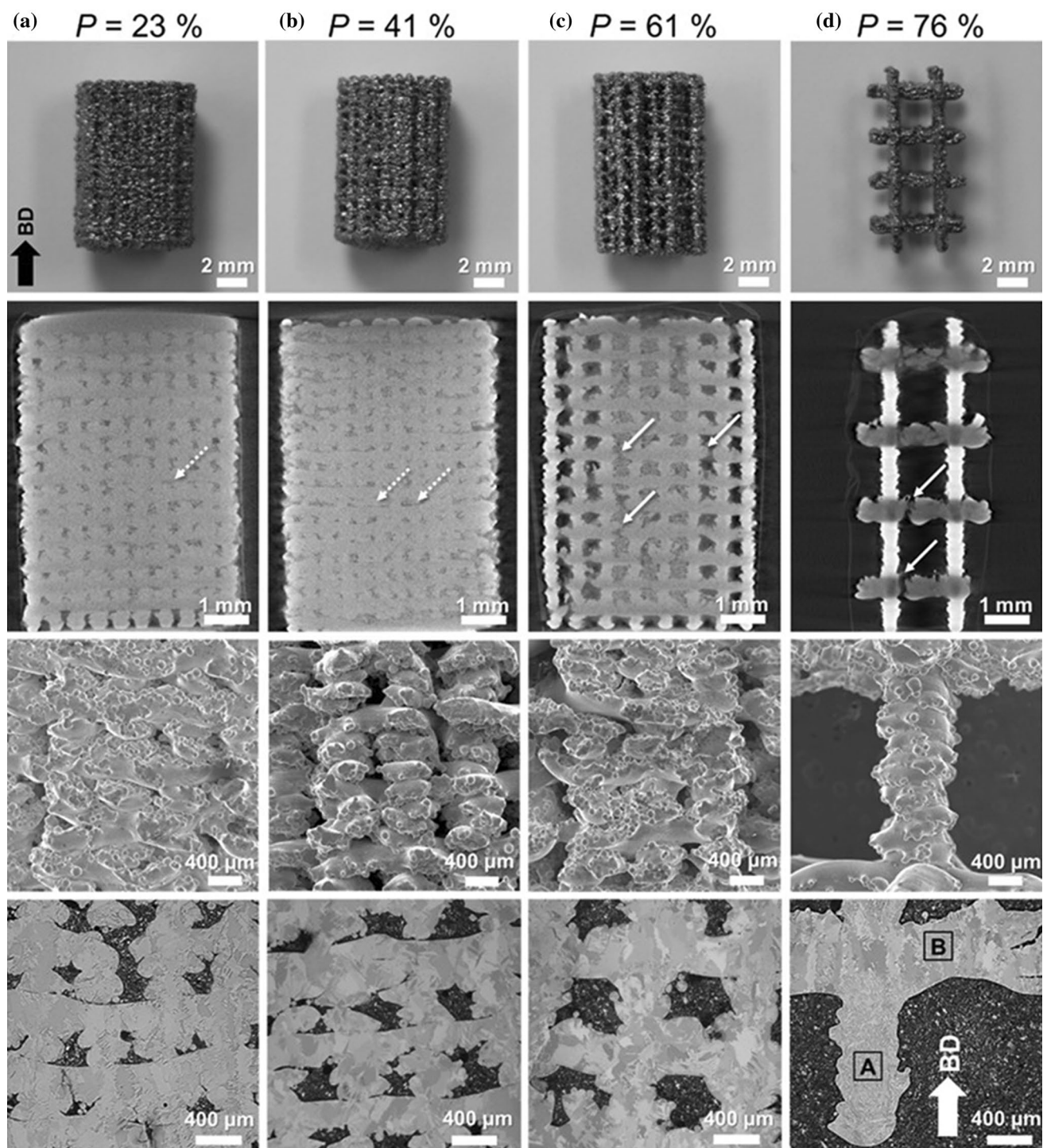


Fig. 4 CP-Ti implants with different porosity (P): **a** photographs, $P=23\%$; **b** micro-CT images, $P=41\%$; **c** SEM, $P=61\%$; **d** optical micrographs, $P=76\%$ [20]

2.3 Dimensional Metrology

Due to the complexity of AM parts, their internal features

cannot be measured by the traditional size measurement technology, and thus CT has played an important role in

the inspection of parts as well as process verification and dimensional measurement since 2011 [23].

2.3.1 CAD Model Validation

In order to verify the geometric consistency of the parts, the CT voxel model of AM parts is usually compared with the original CAD file to evaluate the dimensional deviation from the original design. Kruth et al. [24] studied the application of XCT in dimensional quality control, including the basic principles of CT metrology and measurement uncertainty. The deviation from the nominal geometry was calculated by comparing it with the actual shape. They further outlined the principles of XCT metrology, highlighting various data acquisition strategies as well as problems associated with scatter, beam hardening and edge detection. In addition, the authors also mentioned the lack of reference objects for the purpose of XCT verification and calibration, which significantly restricting the applicability of XCT metrology in AM or related areas. Carmignato et al. [25, 26] summarized the methods of accuracy evaluation of XCT dimensional measurements and discussed performance verification and traceability establishment methods, noting the importance of XCT for size measurement of AM parts.

In addition, since reproducibility and repeatability are the main limitations and challenges for AM parts in current status, some scholars have used artifacts to control the performance of a machine or a process. Kruth [27] was the first to mention a test artifact for comparing AM systems in 1991. Moylan et al. [28] built upon their results, proposed a new version of the NIST test artifact for AM machine evaluation on the basis of summarizing the characteristics of the previous test artifact, and combined with coordinate measuring machine (CMM) and XCT to detect its internal defects [29]. Finally, this new test artifact was successfully manufactured by SLM and electron beam melting (EBM), which indicates that it will become a new standard to test the capability of AM systems. Figure 5 shows the picture of the test artifact made by SLM. Möhring et al. [30] used XCT to measure the size of an artifact, and then compared the original CAD data to draw the manufacturing error (Fig. 6). Combined with simulation, machine analysis and appropriate measurement, the author made a comprehensive evaluation of the ability of the artifact. This lays a foundation for the further applications of the artifact in production engineering research.

2.3.2 Reverse Engineering

The CT method is also widely used in reverse engineering to scan the parts and obtained the CAD model for AM process. Reverse engineering of CT started in the field of biology and then slowly expanded into AM. Cooper et al. [31] used CT scanning for the hollow engine valves made

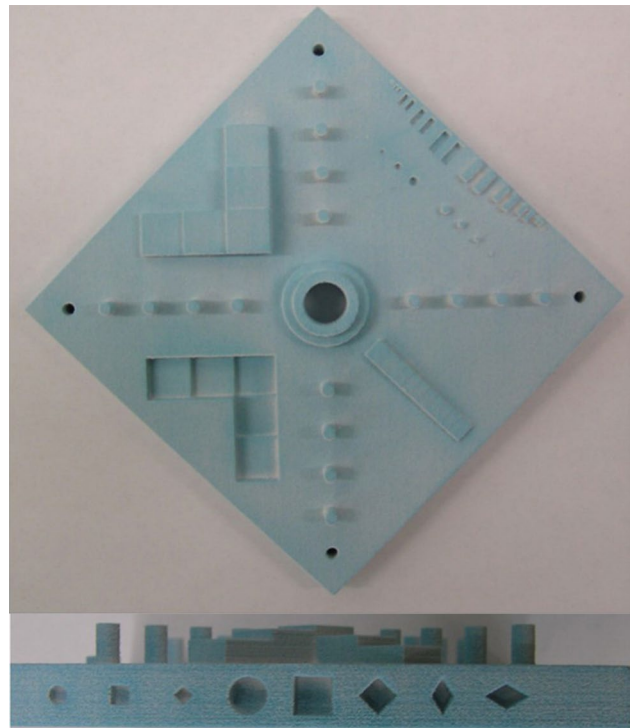


Fig. 5 A test artifact made by AM [28]

by AM, and evaluated the internal geometry and material integrity. The authors found that the part's geometry was well with the CAD model, and had not found significant defects. This is enough to illustrate that XCT is an important tool for validating CAD models. Bauer et al. [32] studied metrological researches on the reverse engineering and repetitive workflow of turbine blades. They made a test component by SLM and performed a CT scanning. The surface deviations and standard deviations of the actual and scanned parts were calculated, and the print parameters were optimized. Figure 7 shows CAD variance analysis of facial implant built by laser-based powder bed fusion (LPBF). Blue areas are smaller than the design, red are larger [9]. Here, reverse engineering quantitatively provides the inaccuracy of manufacturing methods and data acquisition, which helps reduce the cost of replacing new parts.

Enlarging the application of CT metrology in AM parts measurement is the direction to be explored in the future. In order to improve the accuracy of CT measurement, the uncertainty of measurement must be within microns. In addition, a continuation of work regarding XCT system calibration and verification to increase technology adoption, as well as the production of new research regarding XCT measurement of surface texture is also vital to promote the development of dimension measurement in CT.

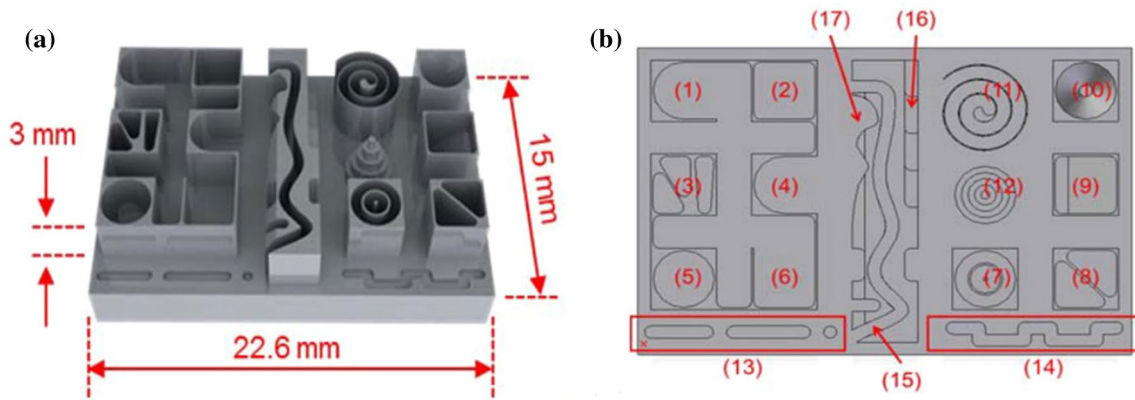


Fig. 6 CAD model **a** and measured geometry sizes **b** of the test artifact [30]



Fig. 7 CAD variance analysis of facial implant built by LPBF [9]

2.4 Characterization of Porosity Defects

In the SLM forming process, the metal parts will experience a complex and non-equilibrium thermodynamic behavior under the action of the laser, and the formability of the parts will be affected by numerous factors. These factors have a significant effect on the microstructure formation and mechanical properties of AM parts. The improper parameters during printing will inevitably lead to the formation of defects such as pores, unfused holes, cracks and so on [33]. The occurrence of defects not only reduces the density of the parts but also deteriorates their comprehensive properties, which significantly restricts the development of AM [34, 35]. Therefore, it is of great importance to elaborately characterize the defects in the AM parts and gain a full understanding of the defects, so as to eliminate or minimize them during AM. Considering the nature of random sampling and a relatively small number of pores, the XCT can provide 3D information about the precise shape and location of the pores in the material. It is more accurate when comparing with the

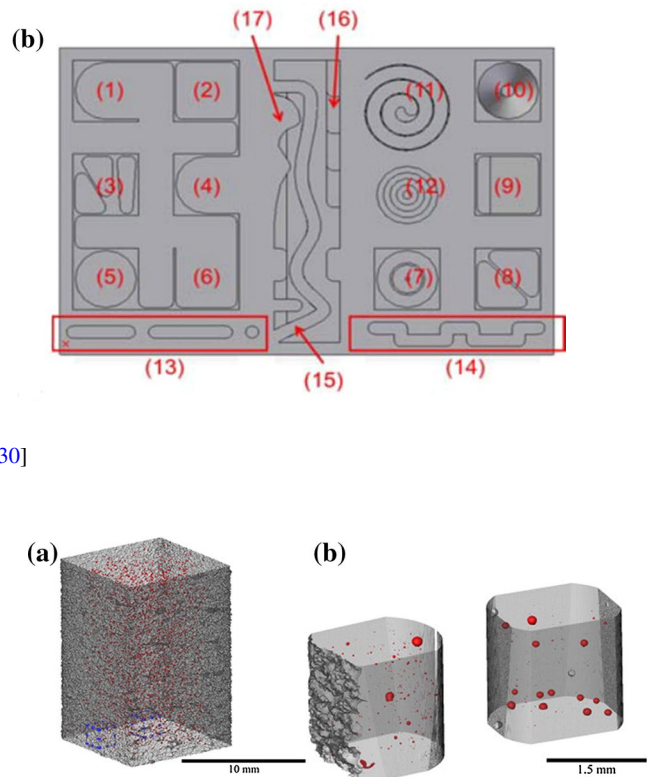


Fig. 8 Examples of XCT datasets. **a** Ti6Al4V sample with a voxel size of 9.9 μm ; **b** the edge and the center of the same sample with a voxel size of 2.1 μm [39]

traditional metallographic method [36]. The application of XCT for the non-destructive measurement of density and porosity, as well as the study of pore morphology and distribution, is now a well-established practice that applies particularly well to the defect characterization of AM parts [37].

Van Bael et al. [38] designed and manufactured porous Ti6Al4V structural samples using SLM, and the empirical correlation functions of pore volume, porosity, specific surface area and designed pore diameter were obtained by CT characterization technology, which lays the foundation for porous structure parts manufactured by SLM. Tammaw-Williams et al. [39] studied the size, volume fraction and spatial distribution of pores in Ti6Al4V samples in detail through XCT, as shown in Fig. 8. They also revealed that pores were not randomly distributed, and the majority of the pores were found to be small spherical gas pores, concentrated in the infill hatching region. They also found that the level of gas porosity could be reduced by increasing the energy density or focus of the electron beam in a certain range [40, 41].

Lacking fusion of planned induced defects in Ti6Al4V parts with different 3D geometric shapes was investigated via non-destructive XCT by du Plessis et al. [42]. As shown in Fig. 9, CT results showed that some melting occurred in the induced defect layer perpendicular to the construction

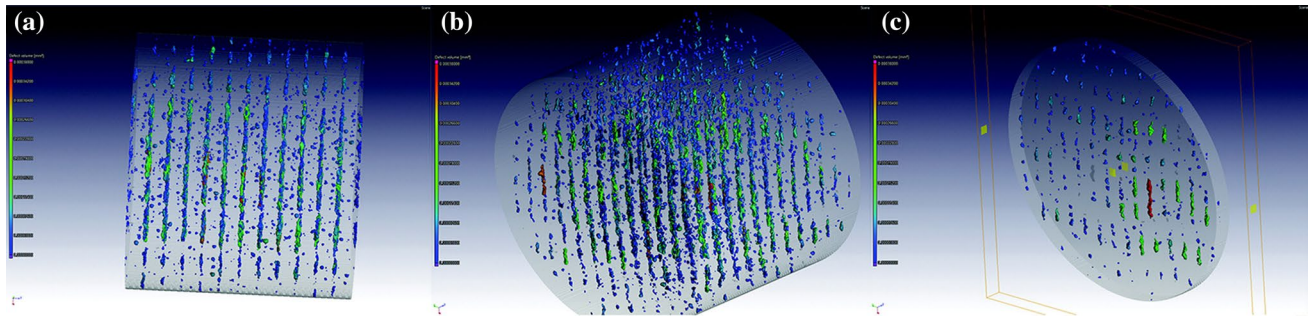


Fig. 9 CT view of porosity varying with the direction of construction. **a**, **b**: two directions and **c** one cropped view to emphasize the directionality of the porosity trails [42]

direction up to 180 μm in height. This indicated that the fusion existed through the fusion layer above the cavity, which minimized the formation of defects in the plane of the build platform. While in the case of vertical cavities parallel to the build direction, much larger defects were observed. In 2019, Neikter et al. [43] used XCT to correlate the defects in Ti6Al4V manufactured by EBM with stress concentration. They found the Ti6Al4V sample had a total of 0.078 vol% defects. The results showed that a majority of the defects were found closer to the surface, which from previous research had been correlated with the process parameter “contouring,” which both the samples were built with. Moreover, from the finite element analysis, the defects showed information on high-stress concentrations, which consequently would lead to crack initiation sites and premature failure. In the same year, Gong et al. [44] utilized XCT to detect defects in Ti6Al4V specimens fabricated via SLM and EBM. The results showed that it was difficult to identify the contour features of SLM defects due to small sizes, but the EBM stochastic defects were large enough to be visualized. In addition, the author also found that the porosity of EBM specimens can be estimated using single slices through image processing, while single slices of SLM specimens only showed a rough texture and could not be used for porosity analysis. An empirical method to approximately estimate the porosity by carefully selecting the neutralization gray threshold was proposed.

Recently, Chioibasus et al. [45] found two kinds of pores in Ti6Al4V through XCT: one is spherical pores caused by local evaporation, and the other is polyhedral pores caused by the lack of overlap between straight lines in the AM process. XCT successfully provided information about the arrangement, location, and size of pores for every varied parameter. Their study confirms that the XCT is an invaluable tool for non-destructive characterization of the printed component for defects evaluation. Likewise, using XCT, Liu et al. [46] elaborately analyzed the spatial and morphological characteristics of pore defects in SLM Ti6Al4V specimens under different processing parameters. They provided

an insight into the influence of process conditions on formation pores or un-melted powder particles during printing. The exhaustive study helps to gain a higher degree of understanding about the mechanism at the base of defects formation. They also discussed in detail, the geometric feature and orientation of the pore relative to the parts and their impacts on tensile properties (Fig. 10).

In addition, aluminum alloy is also one of the common materials widely used in AM. Cai et al. [47] used XCT to measure and characterize the porosity of AlSi10Mg samples prepared by SLM in 2015. The features of porosity based on the XCT image slices illustrated that increasing the laser power in the SLM process would reduce the material porosity level. Porosity-free specimen was obtained at sufficiently high enough laser power at 350 W. The result shows that with the application of the non-destructive XCT method, porosity in the SLM specimens can be measured and characterized by shape and size, to enhance the understanding of the process parameters on material porosity, thereby providing quality control of SLM AlSi10Mg parts. Similarly, through the study of AlSi10Mg pores and unfused voids by XCT, as shown in Fig. 11, Maskery et al. [48] presented a quantitative analysis of the spatial, size and shape distributions of the pores. They found that the largest pore was strongly anisotropic and flat disk-shaped in the XY plane normal to the building direction.

The XCT method was also applied to study the porosity defect in other metallic materials such as 316L stainless steel (SS) and CoCrMo alloy fabricated by SLM. Ziółkowski et al. [49] characterized discontinuity and porosity detection, including the size, shape and orientation of pores in SS316L produced with SLM technology by XCT. Analysis conducted on three produced test samples showed that the application of XCT as a method of quality control of specimens offered a wide range of possibilities to detect porosity within materials. And based on the data obtained by the XCT measurement analysis, it is possible to determine the course of the cracks and diagnose places that may be the point of crack initiation.

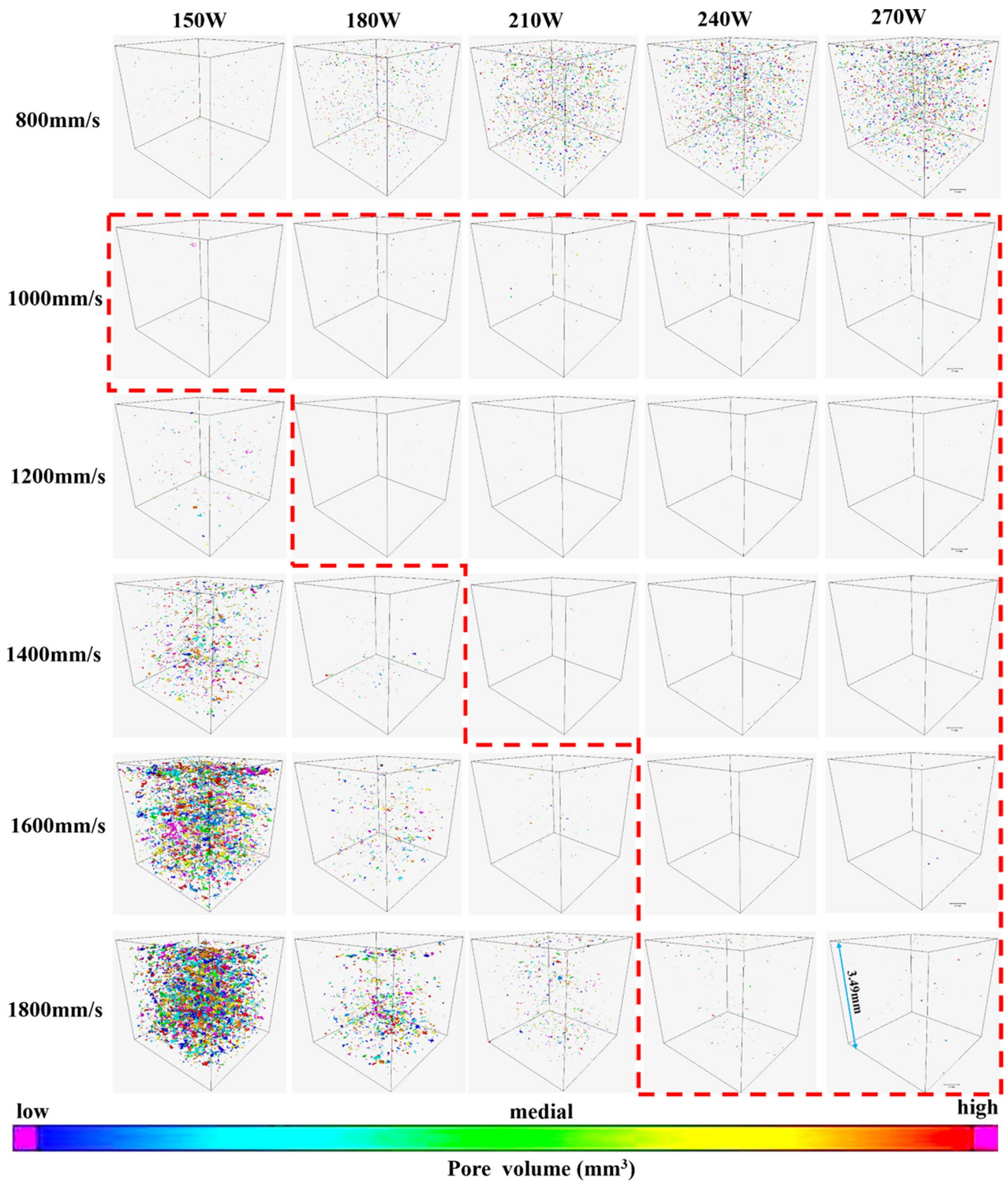


Fig. 10 XCT reconstruction shows the density distribution of Ti6Al4V alloy samples under different laser power [46]

Following this, Zhou et al. [50, 51] used synchrotron X-ray imaging to reconstruct the 3D morphology of SLM defects in the CoCrMo alloy. They illustrated two kinds

of defects in CoCrMo alloy: one is single-layer defects with long and shallow shape, and the other is multilayer defects with small length and width, as shown in Fig. 12.

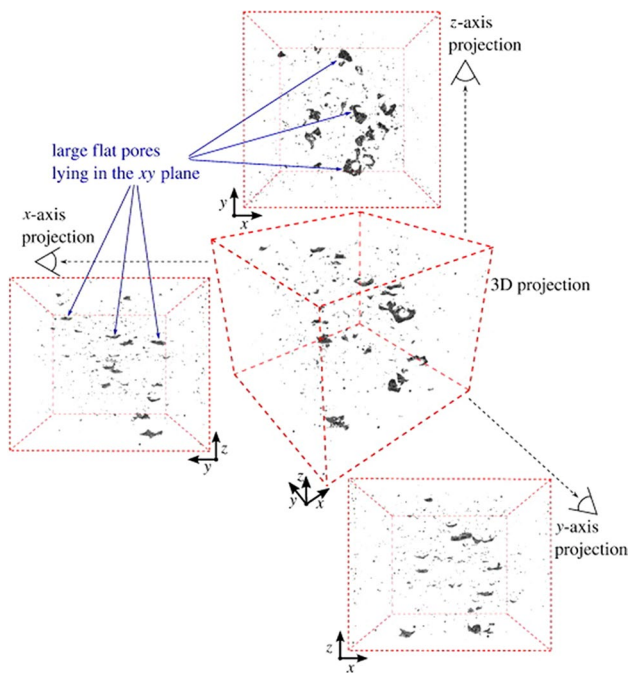


Fig. 11 Pores (dark regions) observed along three principal axes and in 3D projection [48]

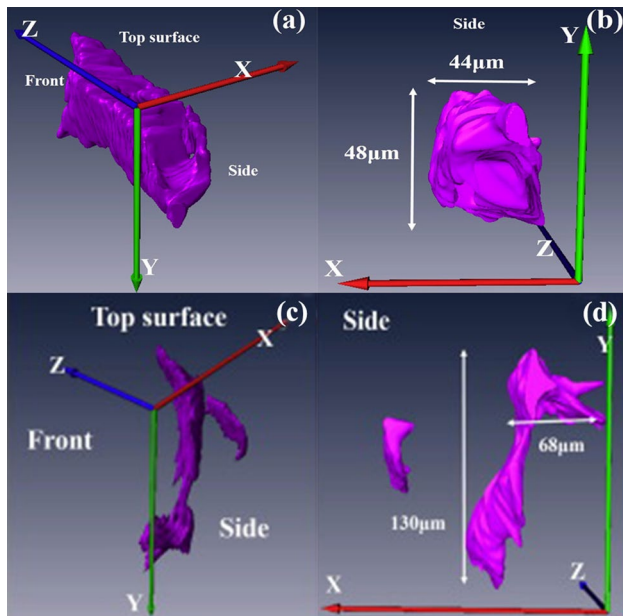


Fig. 12 CT characterization of 3D. **a, b** single-layer defect and **c, d** multiple layers defect morphologies in different directions [50]

The accidental single-layer defects supposed to form as gaps between adjacent laser melt tracks or melt track discontinuousness were attributed to inherent fluid instability under various disturbances. The multilayer defects usually spanned for 2–3 subsequent powder layers on the first

formed single-layer defects. They suggested that the reduction in defect concentration could be achieved by stabilizing the melt pool flow or by reducing the surface roughness by adjusting the processing parameters. Further, Wang et al. [52] studied the internal defects of Mo in wire arc additive manufacturing (WAAM) through state-of-the-art high-resolution CT. As shown in Fig. 13, three main types of defects were revealed: small spherical pores (SSP), inverted pear-shaped pores (IPP) and cavities. By quantitatively and statistically analyze the amount and morphology of the internal defect, the formation mechanisms of different types of defects were proposed and correlated to the fabrication parameters. Specifically, they found IPPs were formed by the collapse of SSPs, which was related to the remelting process. Moreover, the sphericity of the pore was size-dependent. The smaller the pore size, the higher the sphericity. These observations are helpful to explain the defect formation mechanism of Mo manufactured by WAAM.

It is mentioned above that most scholars have studied the influence of process parameters on defects, in which the characteristics and distribution of defects have different effects on the performance of AM parts. In recent years, some scholars have classified the features of defects and explored the relationship between defects characteristics and the performance of AM parts. Sanaei et al. [53] evaluated the correlation between defect features (size, sphericity/circularity, aspect ratio) based on both discussed 2D and 3D defect characterization detection methods. As shown in Fig. 14, they used sphericity and aspect ratio to represent diameter, the projected area of the defects on various planes, defect volume, and defect morphology, providing better visualization of various defect characteristics. Similarly, Liu et al. [46] also characterized four kinds of typical defects of Ti6Al4V in SLM process by CT, and counted pore orientation and spatial distribution under three kinds of energy density. The relationships between fatigue performance and defects features were also discussed. The results showed that the aspect ratio and sphericity of the defects generally decreased as the diameter of the defects increased, making larger defects more critical for fatigue performance. Based on the fast tomography algorithm of convolution neural network (CNN), Zhu et al. [54] divided the 105 holes characterized by XCT of binder jetting copper samples into four morphological groups with different characteristics, and established a comprehensive defect library. In addition, the author used unsupervised learning to effectively divide the detected pores into four morphological groups with obvious characteristics [as depicted in Fig. 15(a)], and quantified the evolution of pore morphology [Fig. 15(b)]. This study is helpful to further develop deep learning algorithms to better represent the topological structure of defects and the potential interaction of adjacent pores in the printed samples inspected by XCT.

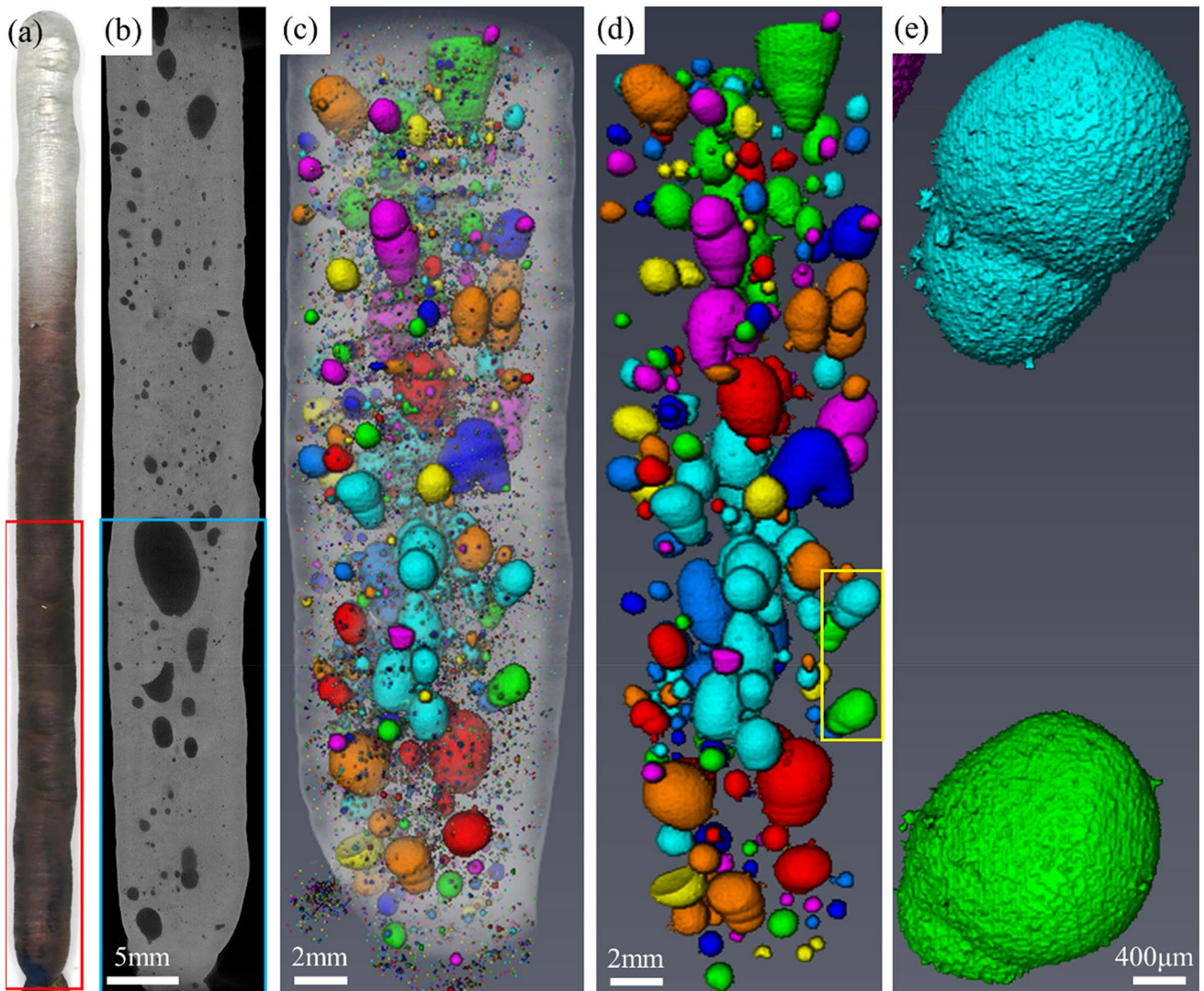


Fig. 13 **a** Peak 1 sample fabricated with $I_p=200$ A and $I_b=60$ A; **b** an original scan tomogram of the red area in **a** ; **c** the reconstructed image of the blue area in **b** ; for better visualization, **d** the image of **c** without the SSPs; **e** the image of the yellow area in **d** [52]

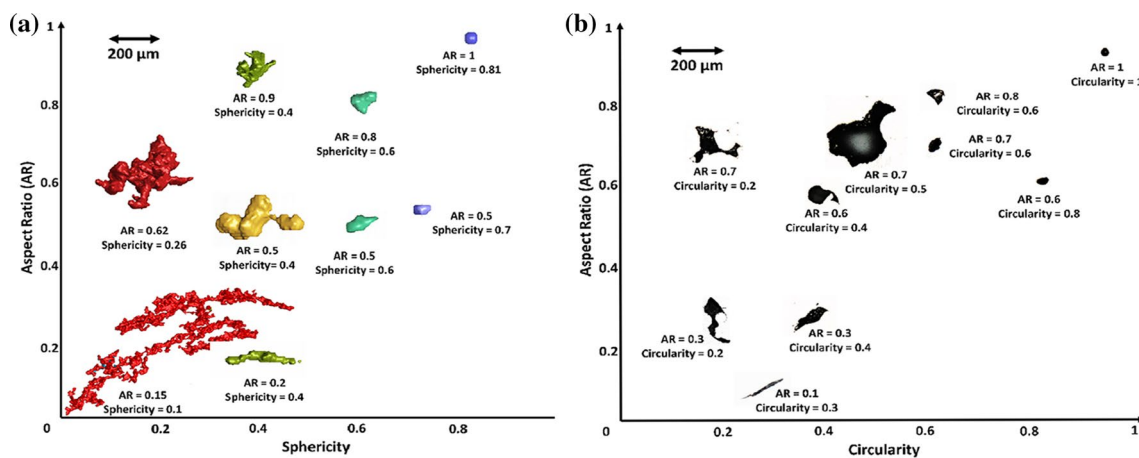


Fig. 14 **a** Aspect ratio (AR) and sphericity visualization of defects gathered from micro-CT results using software for Ti6Al4V AM250 and M290 annealed specimens; **b** aspect ratio (AR) and circularity visualization of defects observed during optical microscopy [53]

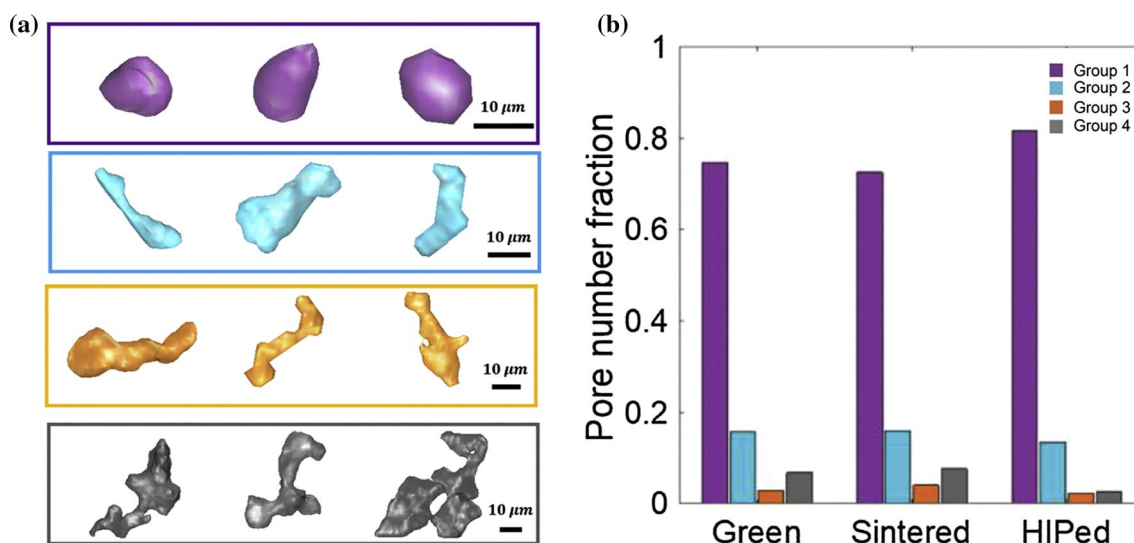


Fig. 15 **a** Four identified pore groups; **b** pore number fraction for the four pore groups [54]

Though XCT is widely used to qualitatively and quantitatively characterize the 3D features of porosity defect in the parts fabricated by AM, it is worth noting that defect analysis is strongly dependent on the threshold value, which directly determines the size, shape as well as morphology of the defects. The automatic determination is not influenced by a human factor; however, in the cases when the volumetric data are measured with insufficient voxel resolution, it gives inaccurate results [55]. It is worth to note that it is difficult for XCT to distinguish the source of small spherical pores inside the build, they may come from the keyhole or the powder. In future work, we should make full use of advanced means such as machine learning and numerical simulation to identify the different characteristics of defects from various angles, and explore the formation mechanism of defects in depth, which is of great significance to enhance the compactness of parts and reduce the formation of defects.

2.5 Mechanical Properties

Compared with the casting parts, the mechanical properties of AM parts are mainly affected by the internal microstructure, complex growth direction and defects of the parts. AM parts have high tensile strength, low ductility and strong anisotropy related to the building direction [56, 57]. XCT can also be applied to characterize the tensile fracture and internal pores of reinforced parts, in order to gain a better understanding of the correlation between the defect features and properties of printed components.

In a study investigating Ti6Al4V manufactured by SLM in 2016, Krakhmalev et al. [58] found that the average porosity was less than 0.0022% (density > 99.9%) by means of XCT. It is demonstrated that pore coalescence was the main

crack formation mechanism in the final fracture with typical cup-and-cone fracture morphology, suggesting that XCT is a powerful method to investigate the impact of defects on the mechanical properties. Carlton et al. [59] performed in situ tensile tests on AM SS316L using synchrotron X-ray imaging to track the damage evolution within the materials. The 3D pore volume, distribution, and morphology in SS at the micrometer length-scale were measured, while tensile loading was applied, as shown in Fig. 16. Although the samples with high porosity were improved by annealing, they still showed poor mechanical properties. They also found that porosity distribution played a more important role in affecting the fracture mechanisms than measured bulk density.

Zekavat et al. [60] studied the effect of preparation temperature on the mechanical properties of fused deposition modeling (FDM) polylactic acid (PLA) filament parts by XCT, and they found that the fracture strain of the sample prepared at lower temperature was larger, but its tensile strength was relatively low. However, the samples prepared in the higher temperature range had higher tensile strength because of the better bonding between extruded fibers. The results showed that different mechanical responses were highly related to the internal geometry of the specimens and not necessarily the porosity. It proves that CT shows great potential as a non-destructive tool for the development of the FDM method. Similarly, Stef et al. [61] proposed a detection method based on 2D fracture and 3D XCT analysis for printed Ti6Al4V. They related the 3D spatial distribution, morphology and orientation of voids to the scanning strategy mode. Their results showed that pores were mainly localized on the overlay zones and supported the lack of energy induced by the lower energy at the periphery of the laser spot as the main formation mechanism of porosity. They unveiled

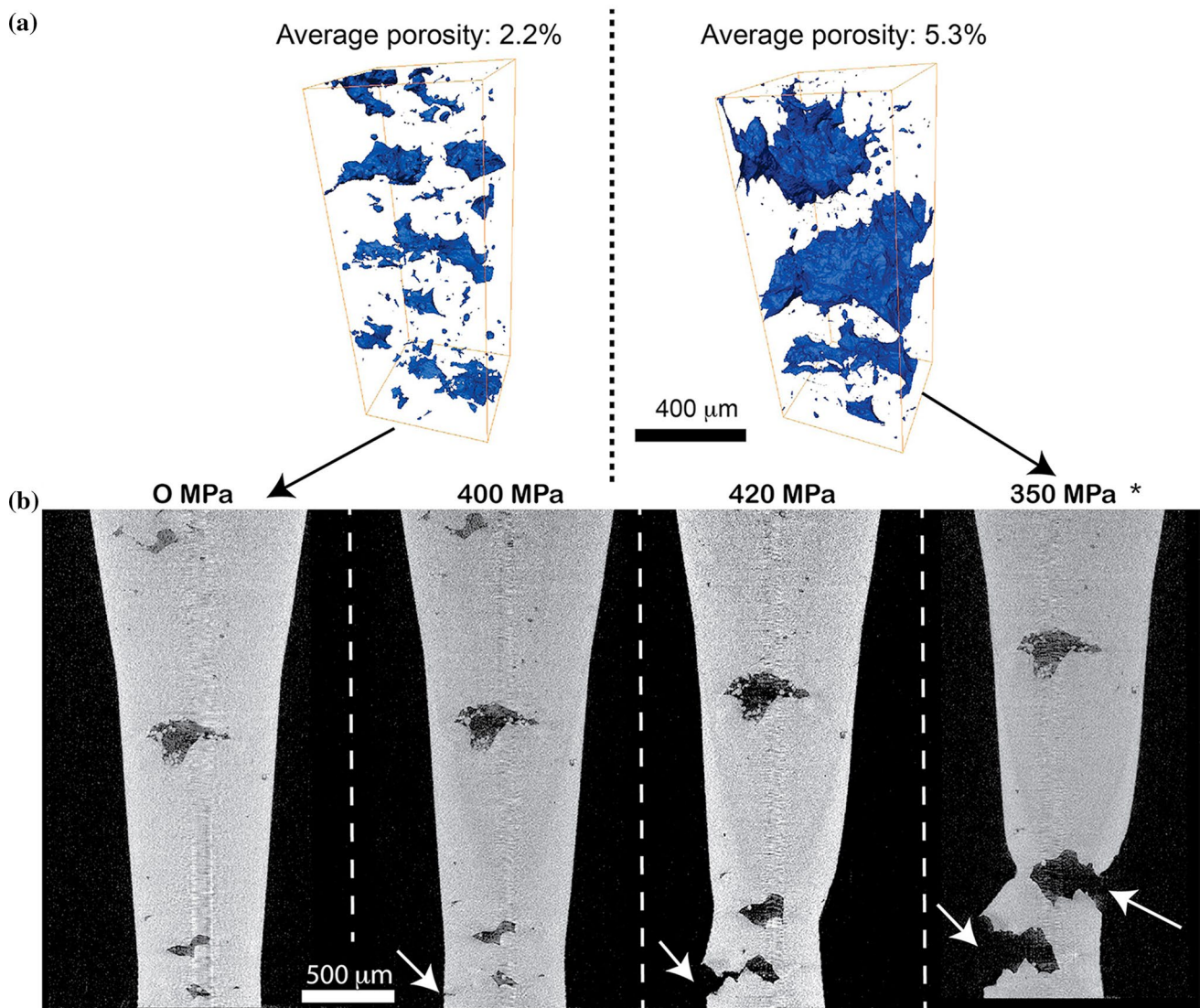


Fig. 16 Results from a high porosity SS316L specimen. **a** 3D rendering of the segmented void distribution for high-porosity AM SS sample before mechanical testing (left) and just before catastrophic failure (right); **b** tomographic images at different load and displacements during tensile loading [59]

that the tensile properties and crack path were affected by the 3D distribution of voids and the crack paths followed the alignment directions of voids, as shown in Fig. 17 where the crack paths are parallel to the building directions. This further confirmed the research of Krakhmalev et al. [58].

For AM parts in the fields of aviation, aerospace, power and energy, many parts are subjected to varying degrees of alternating stress in the course of service, which leads to fatigue failure. It is confirmed that the porosity defects show an important impact on the fatigue performance during the service of AM parts. Siddique et al. [62] used CT to evaluate the effect of stress concentration caused by porosity on the fatigue dispersion in AlSi12 samples. They found that pores were the potential sites of crack initiation,

while samples without porosity only had a surface crack initiation. The effect of pores was supposed to be more pronounced in initiating crack when found in the vicinity of the surface. Based on this, a recommendation by setting the regional remelting of the contours up to 200 μm in the SLM process was proposed for fatigue critical components. They also developed a model describing stress concentration factors (k_t) as a function of pore characteristics (pore diameter and distance from surface) based on the results from CT scans. In the study of Sandgren et al. [63], the fatigue crack growth (FCG) behavior of Ti6Al4V fabricated by laser engineered net shaping (LENS) was observed in situ based on high-energy synchrotron X-ray imaging. As shown in Fig. 18, the crack in Ti6Al4V

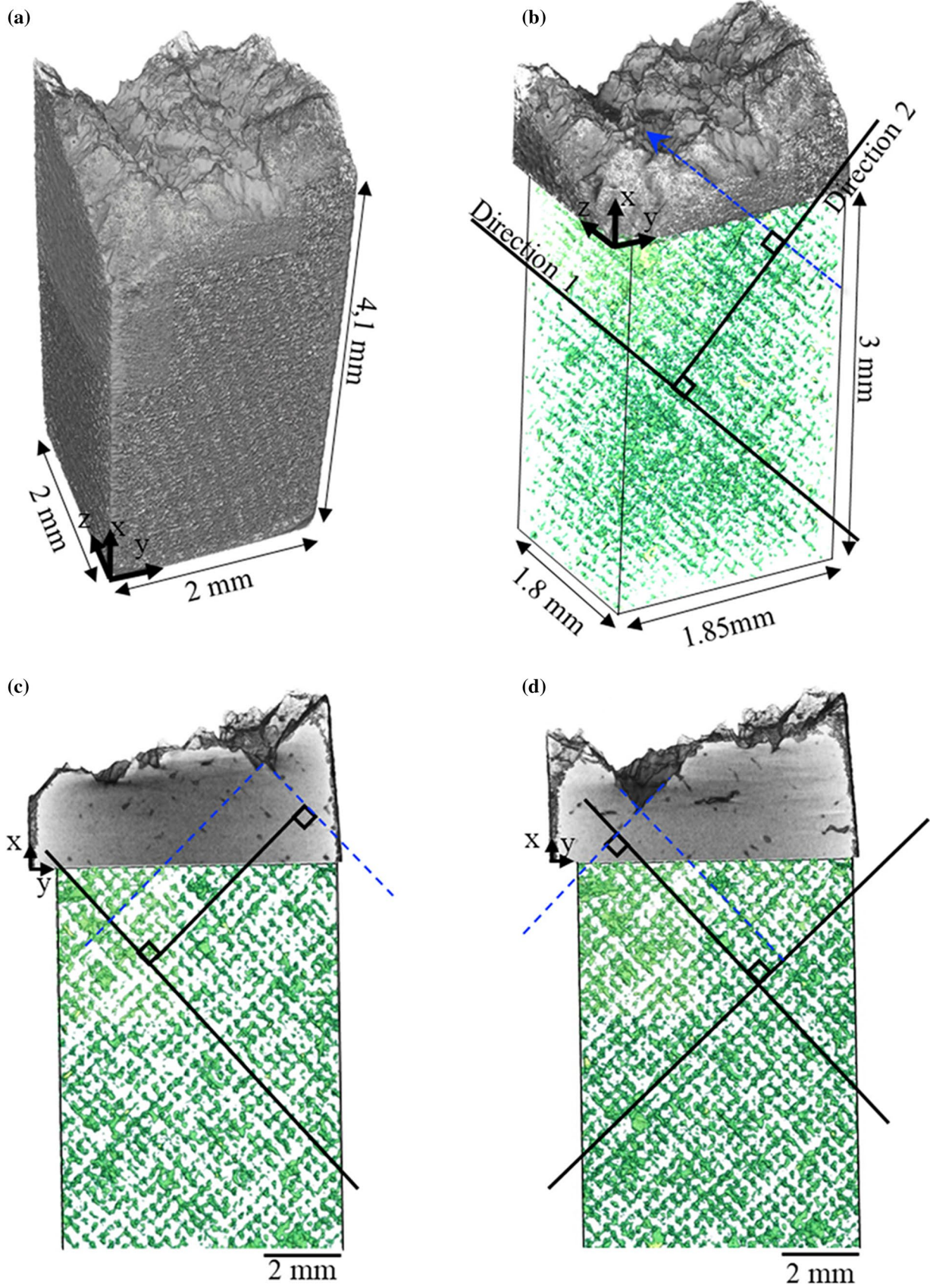


Fig. 17 **a** XCT view of the broken tensile sample along the x -axis; **b** dual-view of the broken tensile sample with the fracture surface at the top part and the 3D void distribution at the bottom part. **c, d**: Two different views of two slices of the fracture surface and the projection of voids on the (XY) plane [61]

martensite mainly grew in-plane, along the tensile axis, emphasizing the importance of local 3D observation and characterization of FCG. The results further confirm that the use of synchrotron X-ray imaging enables a more physically realistic understanding and characterization of the FCG behavior in LENS fabricated Ti6Al4V.

Larrosa et al. [64] analyzed the effect of AM build orientation on porosity and the associated mechanical behavior of SLM manufactured AlSi10Mg samples by means of correlative XCT and other traditional characterization methods (optical microscopy, electron backscatter diffraction, SEM and TEM). They found that the fatigue life was mainly dominated by the existence of pancake-like defects perpendicular to the loading direction, and build samples transverse to the highest fatigue loads might help to enhance the fatigue properties. This research sheds light on the role of defects on the experimental fatigue behavior in the SLM parts to some extent. Based on a self-developed in situ fatigue testing rig fully compatible with the BL13W1 at Shanghai Synchrotron Radiation Facility (SSRF), Wu et al. [65] adopted the Feret diameter and extreme values statistics to characterize the defect size, morphology, population, location and their influence on fatigue life (Fig. 19). The results showed that the fatigue cracks mostly originate on the surface or near the surface of the sample, showing a typical semi-elliptical crack, and the unfused defects had a relatively greater influence on the fatigue life. Compared with the study of Ti6Al4V fatigue behavior by Sandgren et al. [63], they explored the types and growth characteristics of cracks in a more comprehensive way. In addition, the defects less than 50 μm and sphericity of 0.4 ~ 0.65 were proved to be dominant for the fatigue behavior of SLM Ti6Al4V. It is also found that the larger the characteristic size of the defect, the lower the fatigue life. The above conclusions drawn from in situ fatigue test on synchrotron X-ray imaging beamline can provide a theoretical basis and support to predict the fatigue performance of SLM Ti6Al4V.

In a word, the combination of XCT and in situ loading provides comprehensive features (volume, size, distribution, morphology, topology et al.) of porosity defects and their impacts on the mechanical properties of AM parts, as well as the underlying influence mechanism. Those investigations enable us to gain a better understanding of the relationship among the processing parameters, porosity defects and mechanical properties.

3 Online Characterization of AM by Synchrotron X-Ray Imaging

As we all know, the traditional characterization of AM parts is usually performed by postmortem methods. However, this non-in situ detection method will prevent us from studying the microstructure change and defect formation mechanism in the sample during AM. In recent years, synchrotron X-ray in situ characterization technology has been proved to be one of the most effective methods for tracking the defect formation or crack evolution during AM [66]. The third-generation synchrotron radiation source with strong penetration, high space–time resolution and high flux can image parts quickly (millisecond to microsecond). It has natural advantages for studying the evolution of molten pool size and shape, defect formation mechanism and non-equilibrium solidification behavior [67].

AM parts are produced by repeating process via a layer-by-layer manner. When the laser irradiates on the powder, it will inevitably interact with the powder particles, molten pool and metal vapor. This process involves multiple ways of heat transfer, and the hydrodynamic behavior inside the molten pool. Some scholars had better observed the dynamic behavior of the molten pool through synchrotron X-ray imaging, and explored the consolidation mechanism of the powder. Leung et al. [68] used high-speed synchrotron X-ray imaging to reveal the physical phenomena in the process of melt trajectory deposition of the first- and second-layer melt tracks during SLM. They found that there were two main formation mechanisms of the molten pool: one is that the newly formed molten pool promoted the growth of molten pool by wetting with molten beads because the laser beam heated the molten pool while reducing its surface tension; the other is that the laser-induced gas or steam jet pulled the powder particles into the melt trajectory and caused the melt trajectory to grow (Fig. 20). The former was the main mechanism. In addition, the time-resolved quantification of pore and spatter motion also provided key information about its velocity and direction, which was the unique advantage of ultrafast synchrotron X-ray imaging. This is an important step in revealing the causes of pore formation and exploring the interaction between laser and matter. Later, Chen et al. [69] further captured the morphological evolution of each melt track in the five-layer melt trajectory by ultrafast synchrotron X-ray imaging, with the metal vapor jet ejecting droplets and powder spatter vertically from the denudation zone, and small holes were formed in the deposition layer. The phenomenon of keyhole correlation in multilayer structure was similar in all layers. The author's results clarify the mechanism of weld pool growth, which establish the basis for the combination of follow-up and modeling to improve the quality of LPBF parts.

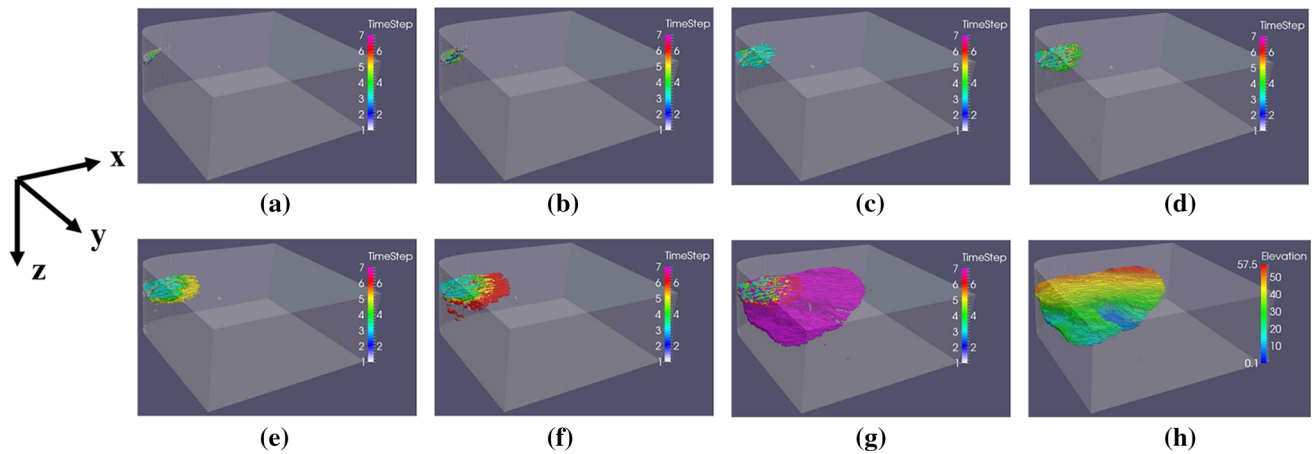


Fig. 18 Snapshots from 3D microtomography reconstructions: **a–g** crack propagation corresponding to the seven tomography scans; **h** crack elevation at various locations [63]

According to the difference of laser energy density, three modes of molten pool formation were summarized by Gong et al. [70–72], one is the unfused mode formed when the energy density was low, the second is the conduction mode when the energy density was moderate, and the third is the keyhole mode when the energy density exceeded a certain critical value. In the actual production process, the keyhole mode was more efficient in transferring laser energy to the powder layer, but if the process parameters were not controlled correctly, the quality of the forming parts would decline due to too many pores, thus reducing its mechanical properties. Therefore, it is particularly important to effectively control the generation and formation mechanism of pores in the keyhole mode.

Zhao et al. [73] was the first to monitor the LPBF process of Ti6Al4V in situ based on high-speed synchrotron X-ray imaging, as shown in Fig. 21. They not only demonstrated many scientifically and technologically significant phenomena, including melt pool dynamics, powder ejection, rapid solidification, and phase transformation, but also revealed the whole process of keyhole formation in Ti6Al4V. The results showed that the closing time of the keyhole was less than 50 μs . The reason for the formation of the keyhole was described in detail: the absorption of laser energy led to the strong evaporation of the surrounding metal, and the recoil pressure gradient was produced by the rapid movement of metal vapor, which made the melt spray. When the laser was turned off, the local negative pressure environment caused the liquid metal to flow to the center of the melting pool. Due to the large depth of the cavity, the liquid metal at the top maintained high horizontal mobility, while the horizontal movement at the bottom was too slow, resulting in the formation of keyhole. On the basis of previous research, Cunningham et al. [74] also determined the threshold from conduction mode

to keyhole mode in 2019, and finally deduced four transformation steps of the keyhole: vaporization, depression of the liquid surface, instability, and then deep keyhole formation. Then they observed the keyhole and found that the boundary of the porosity region was sharp and smooth, and the critical keyhole instability generated sound waves in the molten pool, providing an additional and important driving force for the pores near the tip of the keyhole to be far away from it and became a defect [75]. In addition, the relationship between keyhole depth, front wall angle and laser power density was also discussed.

Later, Guo et al. [76] also pointed out that under constant line energy density (IDE), the melting zone could change from non-molten pool zone to conductive zone, transition zone and keyhole zone in turn. The three dimensions of the molten pool had increased. Importantly, the author found that at a constant IDE level, when the laser power and laser scanning speed increased at the same time, the energy absorption tended to increase, which was an important factor leading to the change of the molten pool. In the same vein, Martin et al. [77, 78] observed the vapor inhibition and surface instability of Al6061 and Ti6Al4V during LPBF by high-speed transmission X-ray imaging, and described the reflection of laser in the vapor depression and the effect of ablation material on the instability, as well as the mechanism of pore formation by surface drive and keyhole drive. This paved the way for their later multi-physical simulation research. For the elimination of the keyhole, the authors thought that changing the laser power at the threshold of keyhole formation could reduce the formation of keyhole. After that they designed a power distribution strategy and successfully eliminated the keyhole when the molten pool orbit was formed. Hojjatzadeh et al. [79] also found that the high thermal capillary force produced by the high-temperature gradient in the laser interaction area could quickly

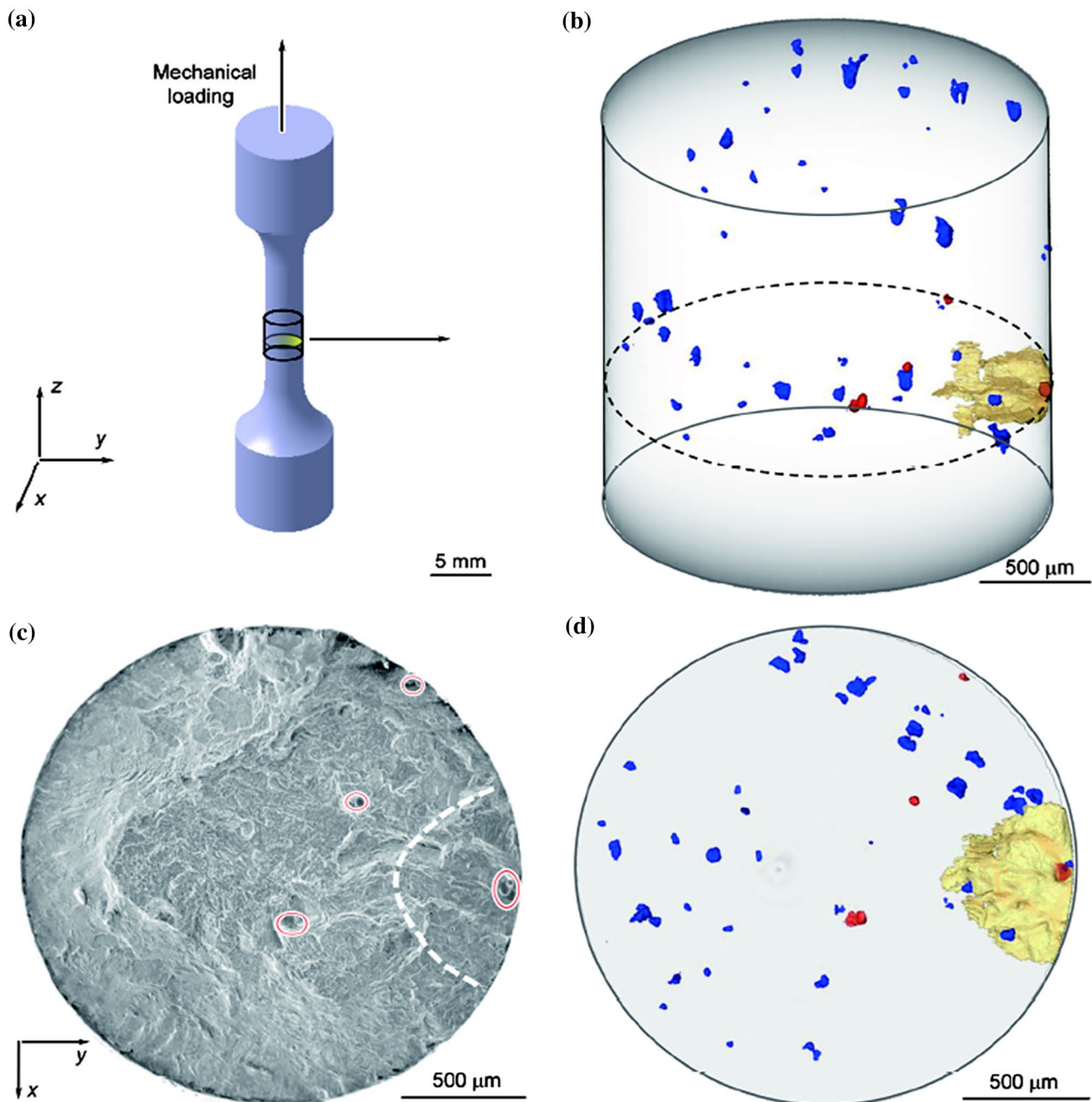


Fig. 19. Three-dimensional reconstruction results of the crack and the fracture morphology of in situ fatigue specimen. **a** 3D XCT of fracture schematic; **b** 3D rendering of defects and crack propagation after 1850 cycle; **c** the fatigue fracture morphology of the specimen at the maximum stress of 1175 MPa; **d** the result of 3D drawing is projected along the direction of principal stress, with yellow representing the crack, blue representing the defect, and red representing the crack surface defect [65]

eliminate the pores in the molten pool during the LPBF process, so as to realize the AM of metal without pores.

In addition to the keyholes formed at the bottom of the molten pool due to recoil pressure, the pores in other locations cannot be ignored. Bobel et al. [80] directly observed the fusion process of AISI 4140 laser powder bed by ultrafast synchrotron X-ray imaging technology. They

considered that the porosity in the accumulation layer mainly came from the trapped gas in the original powder, which was independent of the setting of process parameters (Fig. 22). Through the study of the directional energy deposition process of powder, Wolff et al. [81] found that the flow velocity and distribution of a single particle led to different mechanisms of powder melting, molten pool

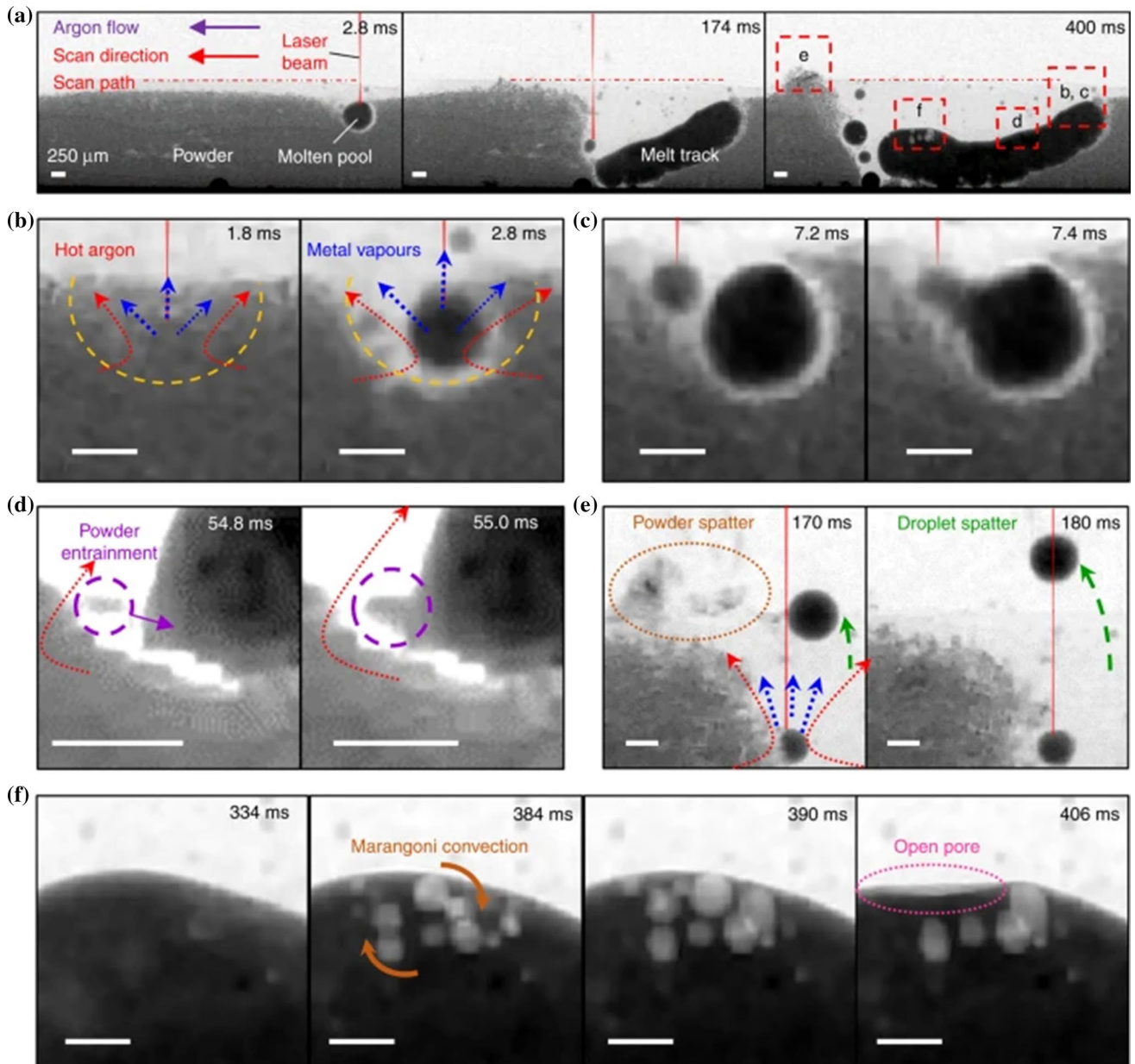


Fig. 20 Time-series radiographs acquired during AM of an Invar 36 single-layer melt track under $P=209$ W, $V=13$ mm s^{-1} and $LED=16.1$ J mm^{-1} . [68]

incorporation and solidification, as well as different pore formation and movement.

During laser-based machining and manufacturing processes, the spatter phenomenon will inevitably occur. This kind of spatter means that the molten material is ejected from the melt pool and deposited in the area near the molten pool, which not only affects the surface roughness of AM parts, but also reduces their quality. Some scholars had made a lot of efforts to reduce the spatter phenomenon of powder beds. Khairallah et al. [82] tried to explain the cause of the spatter. They believed that the surface tension opposite to the

compression effect of the recoil force caused the depression and material spatter. In order to better explain the mechanism of spatter formation, Leung et al. [83] studied the laser-matter interaction of SS316L and 13–93 bioactive glass in the AM process based on ultrafast synchrotron X-ray imaging in 2018. They found that droplet spatter was often formed due to the flow driven by Marangoni in the AM process, which increased the transmission of pores, which further confirms the results revealed by Khairallah et al. [82]. In addition, they also claimed that low viscosity melts such as SS316L were more likely to splash and infiltrate through the

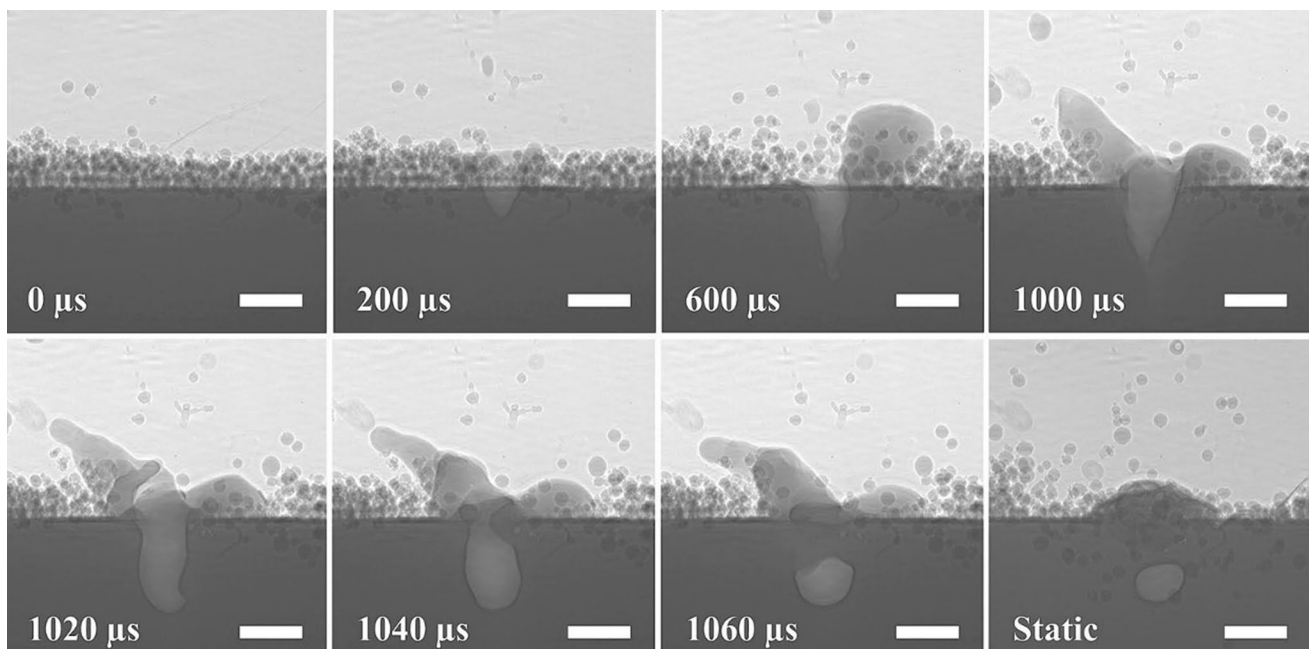


Fig. 21 Dynamic X-ray images of laser powder bed fusion processes of Ti6Al4V. The laser powers are 520 W. The laser beam size is $\sim 220 \mu\text{m}$ ($1/e^2$). The powder particle size is in the range of 5–45 μm , and the powder layer thickness is $\sim 100 \mu\text{m}$. The numbers indicate the time nodes. The laser is turned ON at $t=0$, and continues to heat the sample till $t=1000 \mu\text{s}$. The raw data were taken with a frame rate of 50 kHz. The exposure time for each individual image is 350 ns. All the scale bars are 200 μm [73]

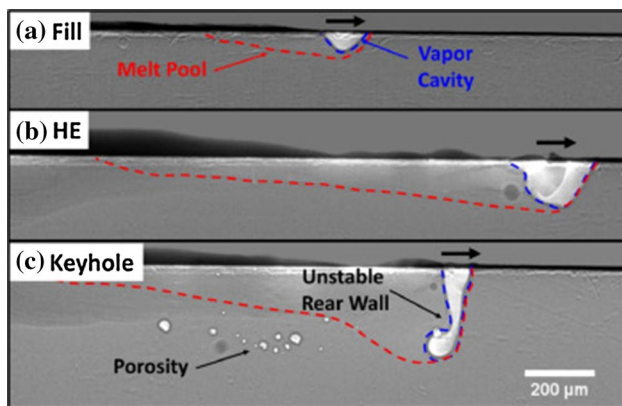


Fig. 22 X-ray images of the melt pool, keyhole and porosity in a 4140 baseplate. **a** Fill; **b** high-energy (HE); **c** keyhole [80]

molten pool to form molten trajectories. On the other hand, the melt with high viscosity would impede the formation of spatter by inhibiting the drive of Marangoni.

Different from the spatter reasons found by the above authors, Guo et al. [84] found that the powder spatter around the laser beam was driven by steam jets. If the particles in the area behind the laser beam were entrapped by the argon flow, the particles in front of the laser beam would also be affected by the argon flow (Fig. 23). Similarly, Matthews et al. [85] used high-speed imaging to

study the denudation of metal powders observed near the laser scan path. They found that the depletion of metal powder particles observed in the zone close to the solidified track was due to a competition between outward metal vapor flux far from the laser spot and the entrainment of powder particles in a shear flow of gas driven by a metal vapor jet at the melt track. This is an important step to predict and minimize the void defects in AM metal components. Anwar et al. [86] observed the transient dynamics of powder spatter during LPBF by in situ high-speed and high-energy X-ray imaging, and quantified the velocity, acceleration and driving force of powder motion induced by metal vapor injection and argon flow. They found that spatter particles were predominantly observed along the scan direction, with minor orthogonal distributions. As the speed of the gas increased, the transport of heavier, bigger splashes increased, resulting in a more even distribution downstream of the gas flow. This lays a good foundation for them to use the discrete phase model (DPM) to study the motion trajectory of spatter particles [87]. Later, Zhao et al. [88] used MHz single-pulse synchrotron X-ray imaging to study the sputtering behavior of Ti6Al4V with micrometer spatial resolution and subnanosecond temporal resolution. Finally, their research revealed a new laser sputtering mechanism: the bulk explosion of a tongue-like protuberance on the front keyhole wall led to ligamentation of molten metal at the keyhole rims and subsequent

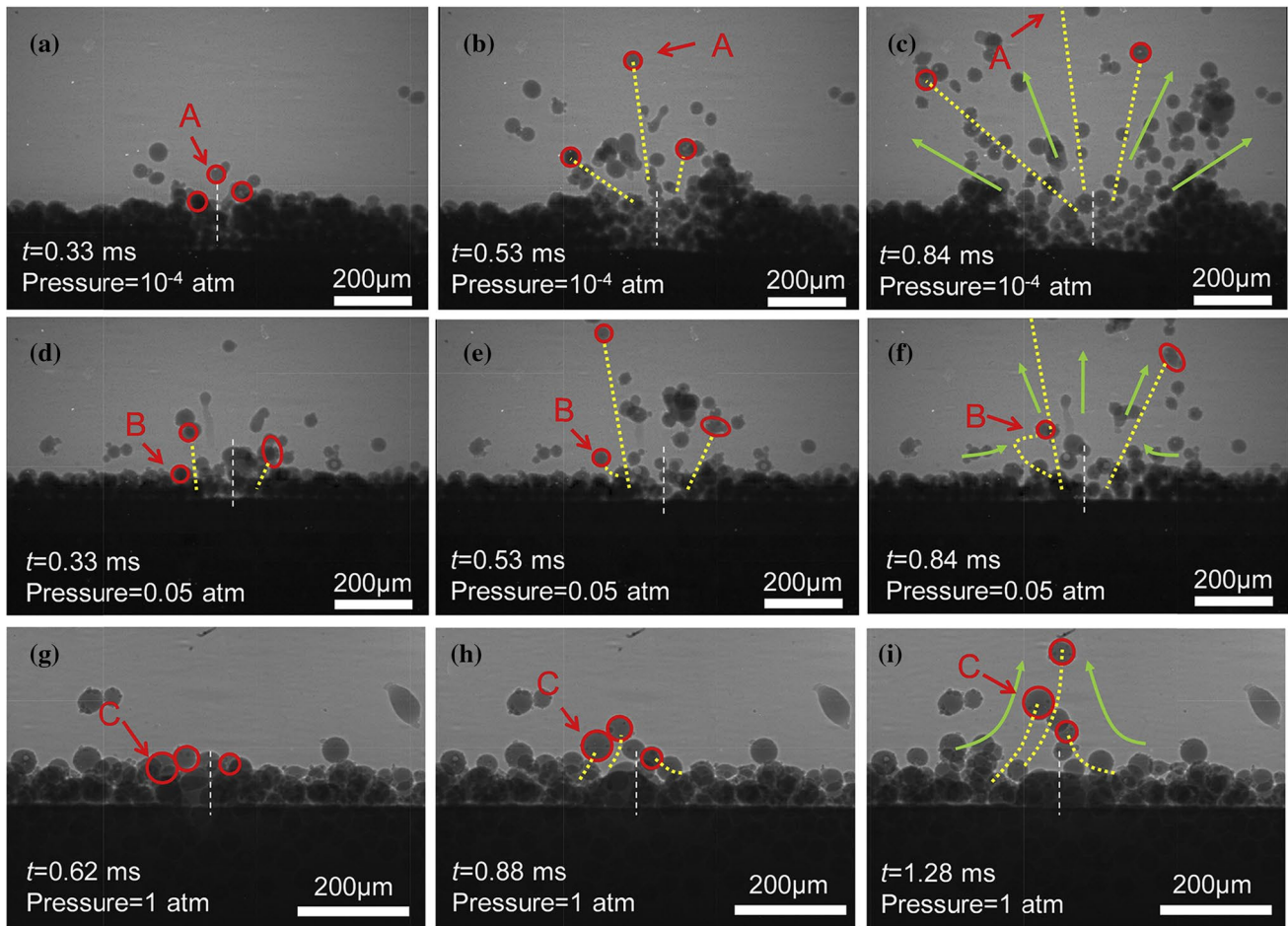


Fig. 23 Dynamic X-ray images showing powder motion at different moments and under different environmental pressures [84]

sputtering. Their study opens a door for the manufacture of spatter and defect-free metal parts via precise control of keyhole dynamics.

Other scholars had also made contributions to the study of other aspects of molten pool formation. Escano et al. [89] reported the powder diffusion kinetics on the particle scale in the powder-bed-based additive manufacturing process and quantified the evolution process of slope velocity, slope roughness and agglomeration dynamics of the powder front. The effect of particle size on powder flow dynamics was revealed. This result is very important for in-depth understanding of the powder diffusion behavior of powder bed in the AM process. Parab et al. [90] quantified the vapor suppression and the fast oscillation of high-speed rotating powder particles for the first time by using the fastest X-ray imaging speed of 6.5 MHz. This is helpful to verify the numerical model, determine the processing conditions, and study the preparation of functionally graded and multi-material products. Calta et al. [91] directly detected the variation of liquid–vapor interface morphology with ambient pressure and oxygen

partial pressure during laser melting of SS316L, Ti6Al4V, Al6061 and Ni400 under the condition of LPBF by in situ X-ray imaging technique. The change in surface tension of the liquid metal related to temperature and composition was found to affect the formation and ultimate morphology of defects in parts of the LPBF. Recently, Chen et al. [92] correlated the manufacturing quality and processing parameters, including powder feeding speed, laser power and transverse velocity, when studying directional energy deposition additives for the manufacture of SS316L, and determined the process conditions needed to suppress the surface disturbance that led to roughness.

With the joint application of crystal imaging and 3D finite element simulation technology based on high-energy synchrotron X-ray source, as well as the development of high-throughput material preparation technology based on AM technology, full-cycle in situ observation and quantitative characterization of AM materials become possible. Synchrotron X-ray imaging will play an important role in the optimization of process parameters and defect tolerance evaluation, which promotes our deeper understanding of AM.

4 Residual Stress Measurement of AM Parts by X-Ray Diffraction

4.1 Sources and Types of Residual Stresses

In the process of SLM forming, a series of complex non-equilibrium physical and chemical metallurgical processes occur under the irradiation of heat flux of Gaussian laser energy distribution, resulting in a complex thermal phase transition field. Mercelis et al. [93] proposed the critical temperature gradient mechanism (TGM) and cooling stage model in 2006, which explained the source of residual stress in parts macroscopically [94]. In the TGM model, after the laser was turned on, the heated metal particles melt rapidly, and the solidification phase tended to expand. As shown in Fig. 24, with the movement of the laser beam, the previous region began to cool and contract, resulting in residual tensile stress in this area. As the parts were manufactured layer by layer, the compressive stress was constantly balanced with the tensile stress [95].

The residual stress can be divided into three types: grain scale, micron scale and nanometer scale. It is difficult to calculate residual stress on the nanoscale by modern measuring methods. Most of the detected residual stresses are on the grain scale, and its macroscopic characteristics will affect the physical properties of the parts.

4.2 Measurement of Residual Stress in AM by X-Ray Diffraction

The measurement of residual stress has been paid more and more attention by researchers. XRD has been widely

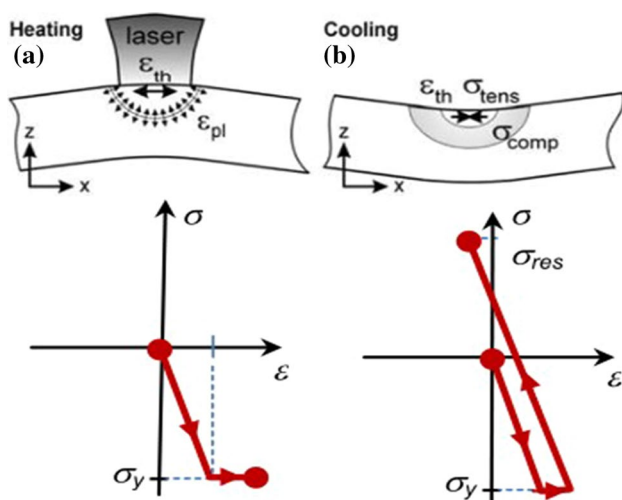


Fig. 24 Residual stress formation model: **a** heating-phase; **b** cooling phase. [95]

recognized as an effective method for residual stress measurement. Simson et al. [96] studied the residual stress of AISI 316L AM parts by XRD in 2017 and examined residual stress at different depths and at two outer surfaces. They found that the residual stress along the scan direction were higher than that in the vertical direction at the top surface of the part. On the contrary, at the lateral surface, the maximum principal stress was perpendicular to the scan direction and paralleled to the building direction. This coincided with the two mechanisms of residual stress generation, namely the TGM and the cool-down phase. In addition, the results also indicated that the dependence of the stress values on the structural density, adherence of non-fused and partly fused powder particles. Later, Marola et al. [97] studied Al stress level both on the surface and in the interior of LPBF AlSi10Mg samples by XRD. It can be concluded that the stress level perpendicular to the building direction was higher, which was due to the lower amount of Al grain boundaries along the building direction. This result is different from the stress maximum position in the Simson's study [96]. Besides, it was also found that the value of stress decreased slightly when increasing the sectioning depth. Their work provides a clear distinction among the stresses occurring in LPBF samples of AlSi10Mg, which has made a certain contribution to the follow-up study of stress.

The residual stress of AM parts is affected by many different process parameters, such as scanning strategy, scanning speed, holding time and so on. The residual strain on Ti6Al4V under different processing parameters was measured by Promopattum et al. [98] using XRD technique. They found that when the scanning length of cubic specimen was 5 and 1 mm, respectively, and the residual stress decreased from 185 to 90 MPa. It proved that the surface temperature could be increased, and the temperature gradient at the solidification front could be reduced by using a shorter scanning vector, thus minimizing the residual stress. This could potentially reduce the need for post-processing as well as decrease a chance of part's failure during production. In addition, Levkulich et al. [99] carried out XRD on the surface of Ti6Al4V samples manufactured by LPBF. They observed that LPBF process parameters (scan speed, laser power, build height, build plan area, and substrate condition) had a great influence on the development of residual stress and deformation in the matrix (Fig. 25). The residual stress on the top surface of LPBF samples could be decreased by increasing laser power, reducing scanning speed and decreasing build plan area. Furthermore, their results provide a valuable foundation for future modeling and simulation of the evolution of residual stress and distortion.

A large number of analyses have proved that the change of temperature with time has a very important influence on the residual stress. Synchrotron X-ray diffraction (SXRD) is a detection method that can monitor the hot working state

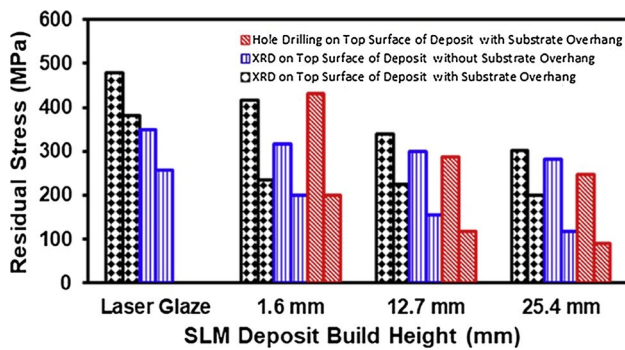


Fig. 25 XRD and hole-drilling principal stress measurements performed on the top surface of deposits with various build heights [99]

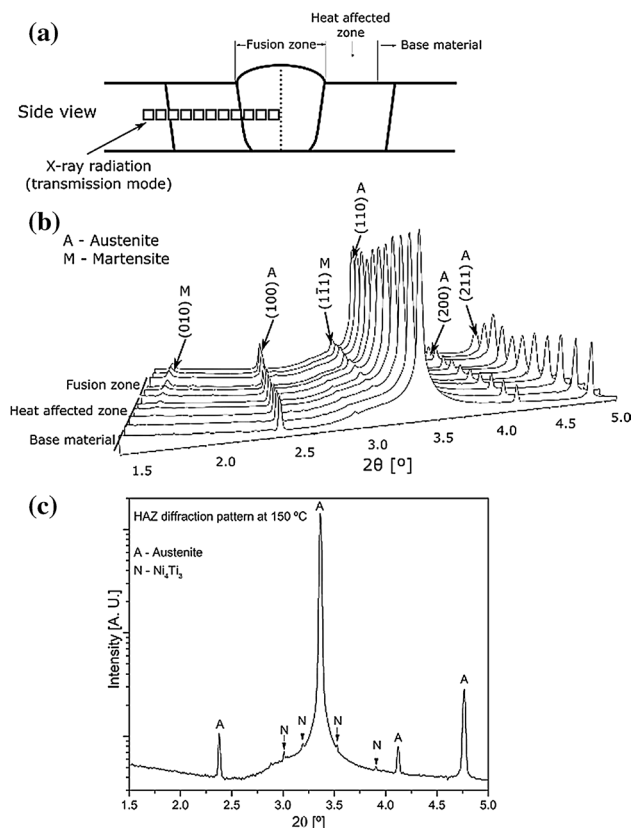


Fig. 26 **a** Schematic representation of the regions probed during the in situ XRD experiments; **b** room temperature X-ray diffraction patterns; **c** diffraction pattern of the HAZ at 150 °C [100]

of parts in real time. In recent years, it is not uncommon to use SXRD to explore the residual stress caused by thermal change in the process of AM. Oliveira et al. [100] used SXRD to determine the local transformation temperatures along the thermally affected regions in a laser processed NiTi thin sheet, as shown in Fig. 26. It was observed that the temperature gradient of phase transition was related to local chemical composition changes caused by Ni depletion

and residual stresses. The new results provide a more fundamental understanding of the microstructure observed in AM parts and its relation to the phase transformation characteristics. Schmeiser et al. [101] studied the strain and stress formation during the manufacturing of multilayer thin walls made from SLM IN625. They found that the correlation between temperature and yield strength led to the maximum stress at 300 μm from the top layer of IN625 sample. The study demonstrates the potential of high-energy SXRD for in situ SLM research.

At present, the research on the residual stress of AM parts is in a stage of rapid development, and the stress field is affected not only by microstructure but also by macroscopic parameters. The above results prove that XRD can better measure the residual stress in the process of AM. In the future, a variety of measurement methods can be used to fully understand the state of residual stress in AM parts, combined with quantitative theoretical models to improve the stress distribution and the quality of parts efficiently.

5 Summary and Future Outlook

In this paper, the studies on the application of synchrotron X-ray imaging and diffraction in AM artifacts are summarized. Since both scientific and technological problems affect the quality and cost of AM products, including defects in typical materials (such as Ti6Al4V and AlSi10Mg), surface roughness, residual stress and so on [102, 103]. By using synchrotron X-ray characterization methods, not only the parts with complex geometry can be analyzed with high precision, but also the main defect information can be detected by rapid scanning or imaging. A better understanding of the formation mechanism of defects and the impact of defects on mechanical performance were achieved, enabling the quality improvement and better post-processing technologies development.

Although the synchrotron X-ray has been widely used in detecting the microstructure, defect formation as well as their evolution processes, opening the door for gaining insight into the AM, further development is still necessary to broaden the application of X-ray in AM process. The development directions in the future are as follows. The online monitoring is still challenge, and the important factors that affect the quality of parts, such as temperature field, velocity field, cooling rate, solidification parameters et al., must be combined with real-time model to reduce defects and improve quality. In addition, online inspection of the real laser printing process with multilayer structure combining ultrafast synchrotron X-ray imaging, high-speed light photography and infrared thermometer is expected in order to reveal the microstructure, fluid convection and temperature field during AM. Also, it is of great significance to verify

and amend the computational numerical model of AM by synchrotron X-ray imaging or diffraction result so as to accurately simulate the non-equilibrium phenomenon in the molten pool during AM process.

Acknowledgements This work was financially supported by the National Nature Science Foundation of China (No. 51701112), the National Key Research and Development Program of China (No. 2019YFA0705300), the Shanghai Rising-Star Program (Nos. 20QA1403800 and 21QC1401500), the Shanghai Science and Technology Committee (No. 19DZ1100704), the open fund of State Key Laboratory of Solidification Processing in NWP (Grant No. SKLSP202107). The authors are grateful for the support from Shanghai Synchrotron X-ray Facility (SSRF) on data analysis.

Declarations

Conflict of Interest The authors declare that they have no conflict of interest.

References

- [1] D. Herzog, V. Seyda, E. Wycisk, C. Emmelmann, *Acta Mater.* **117**, 371 (2016)
- [2] D. Zhang, D. Qiu, M.A. Gibson, Y. Zheng, H.L. Fraser, D.H. StJohn, *Nature* **576**, 91 (2019)
- [3] D.D. Gu, Y.C. Hagedorn, W. Meiners, G.B. Meng, R.J.S. Batista, K. Wissenbach, *Acta Mater.* **60**, 3849 (2012)
- [4] H. Gong, K. Rafi, N.V. Karthik, T. Starr, B. Stucker, Defect morphology in Ti-6Al-4V parts fabricated by Selective Laser Melting and Electron Beam Melting. Paper presented at the 24th annual international solid freeform fabrication symposium, 16 August 2013
- [5] N.T. Aboulkhair, N.M. Everitt, I. Ashcroft, C. Tuck, *Addit. Manuf.* **1–4**, 77 (2014)
- [6] S.E. Zeltmann, N. Gupta, N.G. Tsoutsos, M. Maniatakos, J. Rajendran, R. Karri, *JOM* **68**, 1872 (2016)
- [7] D. He, Z. Wang, M. Kusano, S. Kishimoto, M. Watanabe, *NDT E Int.* **102**, 90 (2019)
- [8] Z. Ding, N. Zhang, L. Yu, W. Lu, J. Li, Q. Hu, *Acta Metall Sin.-Engl. Lett.* **34**, 145 (2021)
- [9] A. du Plessis, I. Yadroitsev, I. Yadroitsava, S.G. Le Roux, *3D Print. Addit. Manuf.* **5**, 227 (2018)
- [10] R. Cottam, J. Wang, V. Luzin, *J. Mater. Res.* **29**, 1978 (2014)
- [11] N. Hoye, H.J. Li, D. Cuiuri, A.M. Paradowska, *Mater. Sci. Forum.* **777**, 124 (2014)
- [12] S. Sun, Q. Hu, W. Lu, Z. Ding, M. Xu, M. Xia, *Acta Metall Sin.-Engl. Lett.* **31**, 668 (2018)
- [13] Z. Wang, A.D. Stoica, D. Ma, A.M. Beese, *Mater. Sci. Eng. A* **707**, 585 (2017)
- [14] Y. Zhan, C. Liu, J. Zhang, G. Mo, C. Liu, *Mater. Sci. Eng. A* **762**, 138093 (2019)
- [15] J. Li, J. Sun, *Acc. Chem. Res.* **50**, 2737 (2017)
- [16] B.E. Warren, *J. Appl. Phys.* **12**, 375 (1941)
- [17] S. Zhao, H. Tang, G. Chen, J. Yin, J. Wang, Y. Ge, *Rare Metal Mat. Eng.* **47**, 3853 (2018)
- [18] X. Zhou, N. Dai, X. Cheng, A. Thompson, R. Leach, *Addit. Manuf.* **40**, 101913 (2021)
- [19] P.D. Wang, H.S. Lei, X.L. Zhu, H.S. Chen, D.N. Fang, *Int. J. Heat Mass Transf.* **144**, 118632 (2019)
- [20] Y.K. Ahn, H.G. Kim, H.K. Park, G.H. Kim, K.H. Jung, C.W. Lee, *Mater. Lett.* **187**, 64 (2017)
- [21] Y. Wen, T. Gao, Y. Zhang, *Acta Metrol. Sin.* **41**, 1077 (2020)
- [22] V.H. Carneiro, S.D. Rawson, H. Puga, P.J. Withers, *Sci. Rep.* **11**, 4974 (2021).
- [23] A. Buratti, J. Bredemann, M. Pavan, R. Schmitt, S. Carmignato, in *Industrial X-Ray Computed Tomography*, ed. by S. Carmignato (Springer, University of Padova, 2018), p. 333
- [24] J.P. Kruth, M. Bartscher, S. Carmignato, R. Schmitt, L. De Chiffre, A. Weckenmann, *CIRP Ann-Manuf. Technol.* **60**, 821 (2011)
- [25] S. Carmignato, A. Pierobon, P. Rampazzo, M. Parisatto, E. Savio, *Ind. Comput. Tomogr.* **161**, 161–172 (2012)
- [26] S. Carmignato, *CIRP Ann-Manuf. Technol.* **61**, 491 (2012)
- [27] J.P. Kruth, *CIRP Ann.-Manuf. Technol.* **40**, 603 (1991)
- [28] S. Moylan, J. Slotwinski, A. Cooke, K. Jurens, M.A. Donmez, *J. Res. Natl. Inst. Stand. Technol.* **119**, 429 (2014)
- [29] S. Moylan, J. Slotwinski, A. Cooke, K. Jurens, M.A. Donmez, Proposal for a standardied test artifact for additive manufacturing machines and processes. Paper presented at the 23rd annual international solid freeform fabrication symposium—an additive manufacturing conference, Austin, August 2012
- [30] H.C. Möhring, P. Kersting, S. Carmignato, J.A. Yagüe-Fabra, M. Maestro, R. Jiménez, A testpart for interdisciplinary analyses in micro production engineering. Paper presented at the 3rd CIRP global web conference, 2015
- [31] D. Cooper, J. Thornby, N. Blundell, R. Henrys, M.A. Williams, G. Gibbons, *Mater. Des.* **69**, 44 (2015)
- [32] F. Bauer, M. Schrapp, J. Szijarto, *Precis. Eng.* **60**, 63 (2019)
- [33] B. Zhang, Y. Li, Q. Bai, *Chin. J. Mech. Eng.* **30**, 515 (2017)
- [34] R. Cunningham, S.P. Narra, T. Ozturk, J. Beuth, A.D. Rollett, *JOM* **68**, 765 (2016)
- [35] R. Cunningham, S.P. Narra, C. Montgomery, J. Beuth, A.D. Rollett, *JOM* **69**, 479 (2017)
- [36] A.B. Spierings, M. Schneider, R. Eggenberger, *Rapid Prototyp. J.* **17**, 380 (2011)
- [37] A. du Plessis, S.G. le Roux, J. Els, G. Booysen, D.C. Blaine, *Nondestruct. Test. Eval.* **4**, 1 (2015)
- [38] S. Van Bael, G. Kerckhofs, M. Moesen, G. Pyka, J. Schrooten, J.P. Kruth, *Mater. Sci. Eng. A* **528**, 7423 (2011)
- [39] S. Tammas-Williams, H. Zhao, F. Leonard, F. Derguti, I. Todd, P.B. Prangnell, *Mater. Charact.* **102**, 47 (2015)
- [40] S. Tammas-Williams, P.J. Withers, I. Todd, P.B. Prangnell, *Metall. Mater. Trans. A* **47**, 1939 (2016)
- [41] S. Tammas-Williams, P.J. Withers, I. Todd, P.B. Prangnell, *Scr. Mater.* **122**, 72 (2016)
- [42] A. du Plessis, S.G. le Roux, G. Booysen, J. Els, *3D Print. Addit. Manuf.* **3**, 48 (2016)
- [43] M. Neikter, F. Forsberg, R. Pederson, M. Antti, P. Åkerfeldt, S. Larsson, *Aeronaut. Aerosp. Open Access J.* **2**, 139 (2018)
- [44] H.J. Gong, V.K. Nadimpalli, K. Rafi, T. Starr, B. Stucker, *Technologies* **7**, 44 (2019)
- [45] D. Chioibas, S. Mihai, M.A. Mahmood, M. Lungu, I. Porosnicu, A. Sima, *Metals* **10**, 1408 (2020)
- [46] W. Liu, C.Y. Chen, S.S. Shuai, R.X. Zhao, L.T. Liu, X.D. Wang, *Mater. Sci. Eng. A* **797**, 139981 (2020)
- [47] X.F. Cai, A.A. Malcolm, B.S. Wong, Z. Fan, *Virtual Phys. Prototyp.* **10**, 195 (2015)
- [48] I. Maskery, N.T. Aboulkhair, M.R. Corfield, C. Tuck, A.T. Clare, R.K. Leach, *Mater. Charact.* **111**, 193 (2016)
- [49] G. Ziótkowski, E. Chlebus, P. Szymczyk, J. Kurzac, *Arch. Civ. Mech. Eng.* **14**, 608 (2014)
- [50] X. Zhou, D.Z. Wang, X.H. Liu, D.D. Zhang, S.L. Qu, J. Ma, *Acta Mater.* **98**, 1 (2015)
- [51] X. Zhou, N. Dai, M.Q. Chu, L. Wang, D.W. Li, L. Zhou, *Int. J. Adv. Manuf. Technol.* **106**, 3 (2020)
- [52] J. Wang, Y. Cui, C. Liu, Z. Li, Q. Wu, D. Fang, *J. Alloys Compd.* **840**, 155753 (2020)
- [53] N. Sanaei, A. Fatemi, N. Phan, *Mater. Des.* **182**, 108091 (2019)

- [54] Y.H. Zhu, Z.L. Wu, W.D. Hartley, J.M. Sietins, C.B. Williams, H.Z. Yu, *Addit. Manuf.* **34**, 101183 (2020)
- [55] A. Zatočilová, T. Zikmund, J. Kaiser, D. Paloušek, D. Koutný, *Solid State Phenom.* **258**, 448 (2016)
- [56] B. Song, X. Zhao, S. Li, C. Han, Q. Wei, S. Wen, *Front. Mech. Eng.* **10**, 111 (2015)
- [57] T. DebRoy, H.L. Wei, J.S. Zuback, T. Mukherjee, J.W. Elmer, J.O. Milewski, *Prog. Mater. Sci.* **92**, 112 (2018)
- [58] P. Krakhmalev, G. Fredriksson, I. Yadroitsava, N. Kazantseva, A.D. Plessis, I. Yadroitsev, *Phys. Procedia* **83**, 778 (2016)
- [59] H.D. Carlton, A. Haboub, G.F. Gallegos, D.Y. Parkinson, A.A. MacDowell, *Mater. Sci. Eng. A* **651**, 406 (2016)
- [60] A.R. Zekavat, A. Jansson, J. Larsson, L. Pejryd, *Int. J. Adv. Manuf. Technol.* **100**, 287 (2018)
- [61] J. Stef, A. Poulon-Quintin, A. Redjaimia, J. Ghanbaja, O. Ferry, M. De Sousa, *Mater. Des.* **156**, 480 (2018)
- [62] S. Siddique, M. Imran, M. Rauer, M. Kaloudis, E. Wycisk, C. Emmelmann, *Mater. Des.* **83**, 661 (2015)
- [63] H.R. Sandgren, Y. Zhai, D.A. Lados, P.A. Shade, J.C. Schuren, M.A. Groeber, *Addit. Manuf.* **12**, 132 (2016)
- [64] N.O. Larrosa, W. Wang, N. Read, M.H. Loretto, C. Evans, J. Carr, *Theor. Appl. Fract. Mech.* **98**, 123 (2018)
- [65] Z. Wu, S. Wu, J. Zhang, Z. Song, Y. Hu, G. Kang, *Acta Metall. Sin.* **55**, 812 (2019)
- [66] Z. Wu, J. Zhang, S. Wu, C. Xie, Z. Song, *Nondestruct. Test.* **42**, 46 (2020)
- [67] J.A. Slotwinski, Additive manufacturing: overview and NDE challenges. Paper presented at the 40th annual review of progress in quantitative nondestructive evaluation, 2014
- [68] C.L.A. Leung, S. Marussi, R.C. Atwood, M. Towrie, P.J. Withers, P.D. Lee, *Nat Commun.* **9**, 1355 (2018)
- [69] Y. Chen, S.J. Clark, C.L.A. Leung, L. Sinclair, S. Marussi, M.P. Olbinado, *Appl. Mater. Today* **20**, 100650 (2020)
- [70] H. Gong, K. Rafi, T. Starr, B. Stucker, Effect of defects on fatigue tests of as-built Ti-6Al-4V parts fabricated by selected laser melting. Paper presented at the 23rd annual international solid freeform fabrication symposium—an additive manufacturing conference, 16 August 2012
- [71] H. Gong, K. Rafi, T. Starr, B. Stucker, The effects of processing parameters on defect regularity in Ti-6Al-4V parts fabricated by selective laser melting and electron beam melting. Paper presented at the 24th annual international solid freeform fabrication symposium, 16 August 2013
- [72] H. Gong, K. Rafi, H. Gu, T. Starr, B. Stucker, *Addit. Manuf.* **1–4**, 87 (2014)
- [73] C. Zhao, K. Fezzaa, R.W. Cunningham, H. Wen, F. De Carlo, L. Chen, *Sci. Rep.* **7**, 3602 (2017)
- [74] R. Cunningham, C. Zhao, N. Parab, C. Kantzos, J. Pauza, K. Fezzaa, *Science* **363**, 849 (2019)
- [75] C. Zhao, N.D. Parab, X.X. Li, K. Fezzaa, W.D. Tan, A.D. Rollett, *Science* **370**, 1080 (2020)
- [76] Q. Guo, C. Zhao, M. Qu, L. Xiong, L.I. Escano, S.M.H. Hojjatzadeh, *Addit. Manuf.* **28**, 600 (2019)
- [77] A.A. Martin, N.P. Calta, J.A. Hammons, S.A. Khairallah, M.H. Nielsen, R.M. Shuttlesworth, *Mater. Today Adv.* **1**, 100002 (2019)
- [78] A.A. Martin, N.P. Calta, S.A. Khairallah, J. Wang, P.J. Depond, A.Y. Fong, *Nat. Commun.* **10**, 1987 (2019)
- [79] S.M.H. Hojjatzadeh, N.D. Parab, W. Yan, Q. Guo, L. Xiong, C. Zhao, *Nat. Commun.* **10**, 3088 (2019)
- [80] A. Bobel, L.G. Hector, I. Chelladurai, A.K. Sachdev, T. Brown, W.A. Poling, *Materialia* **6**, 100306 (2019)
- [81] S.J. Wolff, S. Webster, N.D. Parab, B. Aronson, B. Gould, A. Greco, *JOM* **73**, 189 (2020)
- [82] S.A. Khairallah, A.T. Anderson, A. Rubenchik, W.E. King, *Acta Mater.* **108**, 36 (2016)
- [83] C.L.A. Leung, S. Marussi, M. Towrie, J.D. Garcia, R.C. Atwood, A.J. Bodey, *Addit. Manuf.* **24**, 647 (2018)
- [84] Q.L. Guo, C. Zhao, L.I. Escano, Z. Young, L.H. Xiong, K. Fezzaa, *Acta Mater.* **151**, 169 (2018)
- [85] M.J. Matthews, G. Guss, S.A. Khairallah, A.M. Rubenchik, P.J. Depond, W.E. King, *Acta Mater.* **114**, 33 (2016)
- [86] A.B. Anwar, Q.C. Pham, *Addit. Manuf.* **22**, 86 (2018)
- [87] A.B. Anwar, I.H. Ibrahim, Q.C. Pham, *Powder Technol.* **352**, 103 (2019)
- [88] C. Zhao, Q. Guo, X. Li, N. Parab, K. Fezzaa, W. Tan, *Phys. Rev. X* **9**, 021052 (2019)
- [89] L.I. Escano, N.D. Parab, L. Xiong, Q. Guo, C. Zhao, K. Fezzaa, *Sci. Rep.* **8**, 15079 (2018)
- [90] N.D. Parab, C. Zhao, R. Cunningham, L.I. Escano, K. Fezzaa, W. Everhart, *J. Synchrotron Radiat.* **25**, 1467 (2018)
- [91] N.P. Calta, A.A. Martin, J.A. Hammons, M.H. Nielsen, T.T. Roehling, K. Fezzaa, *Addit. Manuf.* **32**, 101084 (2020)
- [92] Y. Chen, S.J. Clark, Y. Huang, L. Sinclair, C. Lun Alex Leung, S. Marussi, *Mater. Lett.* **286**, 129205 (2021)
- [93] J.P. Mercelis, J.P. Kruth, *Rapid Prototyp. J.* **12**, 254 (2006)
- [94] B. Vrancken, Dissertation, Arenberg Doctoral School, 2016
- [95] C. Li, Z. Y. Liu, X. Y. Fang, Y.B. Guo, Residual stress in metal additive manufacturing. Paper presented at the 4th CIRP conference on surface integrity, 2018
- [96] T. Simson, A. Emmel, A. Dwars, J. Böhm, *Addit. Manuf.* **17**, 183 (2017)
- [97] S. Marola, S. Bosia, A. Veltro, G. Fiore, D. Manfredi, M. Lombardi, *Mater. Des.* **202**, 109550 (2021)
- [98] P. Promopattum, S.C. Yao, *J. Manuf. Process.* **49**, 247 (2020)
- [99] N.C. Levkulich, S.L. Semiatin, J.E. Gockel, J.R. Middendorf, A.T. DeWald, N.W. Klingbeil, *Addit. Manuf.* **28**, 475 (2019)
- [100] J.P. Oliveira, A.J. Cavaleiro, N. Schell, A. Stark, R.M. Miranda, J.L. Ocana, *Scr. Mater.* **152**, 122 (2018)
- [101] F. Schmeiser, E. Krohmer, N. Schell, E. Uhlmann, W. Reimers, *Addit. Manuf.* **32**, 101028 (2020)
- [102] A. D. Plessis, I. Yadroitsava, I. Yadroitsev, *Mater. Des.* **187**, 108385 (2020).
- [103] S.R. Stock, *Int. Mater. Rev.* **53**, 129 (2013)